

Paragenesis of multiple platinum-group mineral populations in Shetland ophiolite chromitite: 3D X-ray tomography and in situ Os isotopes

H. M. Prichard^{a,d}, Stephen J. Barnes^{b*}, C. W. Dale^c, B. Godel^b, and P. C. Fisher^a, G. M. Nowell^c

^a*School of Earth and Ocean Sciences, Cardiff University, Cardiff, CF10 3AT, Wales, UK.*

^b*CSIRO Mineral Resources, Perth, WA, Australia.*

^c*DGC, Department of Earth Sciences, Durham University, Durham, DH1 3LE, UK.*

^d*Deceased, Jan 1 2017.*

*steve.barnes@csiro.au corresponding author

016

Key words:- PGM, PGE, Chromite, X-ray computed tomography, laurite, Shetland ophiolite.

Abstract

Chromitite from the Harold's Grave locality in the mantle section of the Shetland ophiolite complex is extremely enriched in Ru, Os and Ir, at $\mu\text{g/g}$ concentrations. Volumes were collected on micro-cores from these chromitites using high-resolution X-ray computed tomography have been processed to determine the location, size, distribution and morphology of the platinum-group minerals (PGM). There are five generations of PGM in these chromitites. Small (average $5\ \mu\text{m}$ in equivalent sphere diameter, ESD) euhedral laurites, often with Os-Ir alloys, are totally enclosed in the chromite and are likely to have formed first by direct crystallisation from the magma as the chromite crystallised. Also within the chromitite there are clusters of larger ($50\ \mu\text{m}$ ESD) aligned elongate crystals of Pt-, Rh-, Ir-, Os- and Ru-bearing PGM that have different orientations in different chromite crystals. These may have formed either by exsolution, or by preferential nucleation of PGMs in boundary layers around particular growing chromite grains. Thirdly there is a generation of large ($100\ \mu\text{m}$ ESD) composite Os-Ir-Ru-rich PGM that are all interstitial to the chromite grains and sometimes form in clusters. It is proposed that Os, Ir and Ru in this generation were concentrated in base metal sulfide droplets that were then re-dissolved into a later S undersaturated magma, leaving PGM interstitial to the chromite grains. Fourthly there is a group of almost spherical large ($80\ \mu\text{m}$ ESD) laurites, hosting minor Os-Ir-Ru-rich PGM that form on the edge or enclosed in chromite grains occurring in a sheet crosscutting a chromitite layer. These may be hosted in an annealed late syn- or post magmatic fracture. Finally a few of the PGM have been deformed in localised shear zones through the chromitites.

33 The vast majority of the PGM – including small PGM enclosed within chromite, larger interstitial
34 PGM and elongate aligned PGM – have Os isotope compositions that give Re-depletion model ages
35 approximately equal to the age of the ophiolite at ~492 Ma. A number of other PGM – not confined
36 to a single textural group – fall to more or less radiogenic values, with four PGM giving anomalously
37 unradiogenic Os corresponding to an older age of ~1050 Ma. The $^{187}\text{Os}/^{188}\text{Os}$ isotopic ratios for PGM
38 from Cliff and Quoys, from the same ophiolite section, are somewhat more radiogenic than those at
39 Harold's Grave. This may be due to a distinct mantle source history or possibly the assimilation of
40 radiogenic crustal Os.

41

1. INTRODUCTION

1.1 Platinum-group elements and Os isotopes in ophiolites

42 The study of the Re-Os isotopic system has become an important and widely used tool in
43 investigations of mantle reservoirs and their evolution through Earth history. Owing to the mobility
44 of Re during fluid interactions (e.g. Xiong, 2006), there is great benefit in measuring Os isotopes in
45 situ in Re-poor grains to minimise uncertainties in correction for radiogenic Os ingrowth. Hence a
46 number of studies (e.g. Walker et al., 2002b, González-Jiménez *et al.*, 2014) have taken this
47 approach using Os-Ir rich phases in mantle rocks, particularly chromite-rich rocks in ophiolite
48 complexes. Such IPGE enriched chromitites have attracted much interest since the advent of Os
49 isotope analysis, in that they provide data points constraining the Re-Os mantle growth curve and
50 provide insights into the evolution of mantle reservoirs with time (e.g. Shirey and Walker, 1998).
51 However, the mechanisms by which IPGE are concentrated within ophiolitic chromite remain a
52 matter of debate, resolution of which is critical for the interpretation of the isotope data.

54 Podiform chromitite in ophiolite complexes commonly hosts Ir-, Ru- and Os-bearing platinum-group
55 minerals (IPGM) as for example in the Tiebaghi ophiolite in New Caledonia (Page et al., 1982), various
56 ophiolite complexes in Newfoundland (Page and Talkington, 1984), the Semail ophiolite (Augé 1986,
57 Prichard et al., 1996; Ahmed and Arai, 2003), the Troodos ophiolite in Cyprus (Constantinides et al.,
58 1980; Prichard and Lord, 1990), the Luobusa Ophiolite in Southern Tibet (Zhou et al., 1996), the
59 Kamuikotan zone in northern Japan (Arai et al., 1999) and in the Vourinos and Orthrys ophiolites in
60 Greece (Economou-Eliopoulos, 1996). *In situ* Os isotope measurements have been applied to a
61 number of these. On the whole, as expected, minerals in ophiolites give Re-Os model ages that are
62 the same as that of the formation of the oceanic crust that becomes the ophiolite on emplacement.
63 Some model ages are much older and appear to record a history prior to ocean crust formation with
64 inherited depletion ages from previous melting events. González-Jiménez et al. (2014) review the
65 evidence from *in situ* analysis of individual platinum-group minerals in ophiolitic chromitites and
66 demonstrate that such grains may have highly variable Os isotope compositions. In some cases they

67 show that variable isotopic composition occurs in PGMs located within the same thin section. Thus,
68 in some ophiolitic chromitites the PGM found in a single chromite deposit may show a spectrum of
69 compositions that could be interpreted as Re-depletion (T_{RD}) model ages. This poses an intriguing
70 problem in the interpretation of such data.

71 Some of the highest concentrations of Ir, Ru and Os (IPGEs) are found in the Unst Ophiolite in
72 Shetland. The Shetland ophiolite belongs to the relatively rare group of ophiolites having chromitites
73 that contain elevated Pt, Pd and Rh (PPGE). Examples of these PPGE enriched ophiolitic chromitites
74 include Thetford Mines in Canada (Corrivaux and Laflamme, 1990), Leka in Norway (Pedersen et al.,
75 1993), Albanian ophiolites (Ohnenstetter et al., 1999), Al 'Ays in Saudi Arabia (Prichard et al., 2008a),
76 Bragança in Portugal (Bridges et al., 1993), Pindos in Greece (Prichard et al., 2008b), Pirogues in New
77 Caledonia (Augé et al., 1998), Acoje in the Philippines (Bacuta et al., 1988; Orberger et al., 1988) and
78 Berit in Turkey (Kozul et al. 2014). Chromitites from the Shetland ophiolite belong to the IPGE and
79 PPGE enriched group, with all six PGE being present at $\mu\text{g/g}$ levels. Prichard et al. (2008a) and
80 Prichard and Brough (2009) concluded that the Shetland chromitites formed from magmas that were
81 close to sulfide liquid saturation, resulting in local accumulation of traces of strongly PGE-enriched
82 sulfide liquid.

83 The Shetland occurrences, particularly the very highly IPGE enriched chromitites at Harold's Grave
84 (Fig. 1), provide an opportunity to investigate the processes that lead to IPGE concentration and
85 IPGM crystallisation in ophiolitic chromitite and also to investigate the detailed controls on the
86 variability of Os isotope signatures at grain scale. In this contribution, we use detailed 2D and 3D
87 petrographic observations at high spatial resolutions to address the grain-scale spatial distribution of
88 PGM within the Harold's Grave chromitite. This is the first time that grain-scale 3D spatial
89 information has been combined with *in situ* Os isotope data to investigate the origin of the IPGE
90 enrichment and PGM formation and also the extent of grain scale isotopic heterogeneity and its
91 significance. Our conclusions have implications for the phenomenon of PGE concentrations in
92 ophiolitic chromitites and the mechanisms of concentration of PGEs in Reef-type deposits in layered
93 intrusions, and also provide significant insight into the broader behaviour of the PGEs in mantle
94 processes.

95 **1.2 Platinum-group elements in the Shetland ophiolite**

96 The Shetland ophiolite is exposed in obduction nappes on Unst and Fetlar, the most northerly islands
97 of the Shetland Islands, NE of the Scottish mainland, UK. The lower parts of an ophiolite sequence
98 are preserved with mantle harzburgite overlain by crustal dunite, wehrlite and clinopyroxenite. In
99 turn these lithologies are overlain by gabbro, with dyke swarms above that mark the base of the
100 sheeted dyke complex (Flinn, 1985; Prichard, 1985). The formation of the ophiolite occurred in an

101 ocean that opened at about 600 Ma and closed at about 500 Ma, obducting the ophiolite which was
102 then affected by the intrusion of the Skaw granite in northern Unst at about 425.6 Ma (Flinn and
103 Oglethorpe 2005). A zircon U-Pb crystallisation age of 492 ± 3 Ma from an anatectic plagiogranite vein
104 is accepted as the likely crystallisation age of the ophiolite, which was emplaced during closure of
105 the Iapetus Ocean in the Grampian orogeny at ~ 470 Ma (O'Driscoll *et al.*, 2012).

106 The ophiolite hosts podiform chromitites surrounded by a dunite envelope in mantle harzburgite.
107 Two of these, within the Baltasound area on Unst (Fig. 1), have particularly anomalously high $\mu\text{g/g}$
108 values of PGEs: The Cliff locality is extremely enriched in Pt, Pd and Rh compared with ophiolitic
109 chromitites worldwide; whereas, in contrast, the Harold's Grave locality is IPGE enriched (Table 1),
110 both containing total PGE concentrations in excess of 60 $\mu\text{g/g}$ (Prichard and Lord, 1993). The PGE
111 concentrations in the ophiolite and the history of their discovery are summarised in Brough *et al.*
112 (2015). Detailed petrogenetic studies of the various chromitite pods within the Baltasound area
113 highlight significant short-range variability in chemical and Os isotopic characteristics, implying
114 derivation for a source with short-range heterogeneity feeding magmas through a series of distinct
115 conduits (O'Driscoll *et al.*, 2012; Derbyshire *et al.*, 2013).

116 **1.3 Platinum-group elements and chromitite at Harold's Grave**

117 The Harold's Grave chromitite is located to the north of Baltasound, west of the road from
118 Baltasound to Haroldswick (Fig. 1), within one of the largest dunite lenses in the mantle section of
119 the ophiolite. The chromitite has been quarried and now is present mostly in spoil tips beside a
120 quarry that is 15 m long and 2-3 m wide. However the surrounding dunite contains a few thin layers
121 of chromitite that are still preserved *in situ*. The boulders of spoil show that the chromitite forms
122 parallel layers a few cm thick and around 10 cm apart, separated by dunite. These chromitite layers
123 are typically folded and fractured.

124 The composition of the chromitite at Harold's Grave has been shown to be distinct from the other
125 chromitites in the ophiolite, having lower Mg#, a lower $\text{Fe}^{3+}/\text{Fe}^{2+}$ ratio and elevated concentrations
126 of TiO_2 , V_2O_5 and Zn. These features are consistent with low oxygen fugacity conditions that favour
127 the precipitation of the IPGE into PGM, due to the reduced solubility of the IPGE in silicate melts
128 (Borisov and Palme, 1995, 2000; Brenan and Andrews, 2001; Brenan *et al.*, 2005). Chromites imaged
129 using high resolution X-ray computed tomography display distinctive stepped "hopper" grain
130 boundaries suggestive of rapid crystallisation (Prichard *et al.*, 2017). Analysis of eight chromitites
131 from Harold's Grave suggests that the chromitite is consistently enriched in IPGE with values ranging
132 from 2-7ppm Ru, 1-3ppm Ir and 0.6-3 ppm Os. PPGE are also concentrated in these chromitites but
133 at lower levels than the IPGE with ranges of 420 - 785 ppb for Pt, 257-422ppb for Rh and even lower

134 values of 36-69 ppb for Pd. The samples chosen to study in this current research were those
135 analysed for whole rock PGE as described in Brough et al. (2015) (Table 1).

136 **Fig 1**

137 **1.4 Platinum Group Minerals in the Shetland ophiolite**

138 There has been a number of studies of PGM in the Shetland ophiolite. PGM located in different
139 stratigraphic levels and in different chromitite pods within the mantle have been summarised in
140 Prichard et al. (1994). (Note that we follow the convention of using the abbreviation PGM to refer to
141 platinum-group-element dominant minerals, PGE to refer to the elements, IPGE to refer to Ir, Ru and
142 Os, and IPGM for IPGE dominated minerals). PGM in the Cliff and Harold's Grave chromitites are
143 described in Prichard and Tarkian (1988) and Tarkian and Prichard (1987). At Cliff the PGM
144 assemblage consists of sperrylite $PtAs_2$, stibiopalladinite Pd_5Sb_2 , hongshiite $PtCu$, PGE and Au alloys,
145 potarite $PdHg$, and Pt- and Pd-oxides as well as Os-, Ir- and Ru-rich PGM (IPGM) including laurite
146 (RuS_2), irarsite (Ir,Ru, Rh,Os)AsS, hollingworthite (Rh,Pt,Pd)AsS, and native Os all accompanied by
147 ruthenian pentlandite (pentlandite with > 50 mg/g Ru). Except for Harold's Grave, the rest of the
148 chromitite pods in the mantle harzburgite are not enriched in PGE above the 10-100 ng/g levels
149 expected for most podiform chromitites. Occasional composite grains of PGM do occur, as in the
150 chromitite pod at Nikkavord North which contains clusters of laurite, irarsite, hollingworthite,
151 ruthenian pentlandite, Ni-Rh antimonide and native Os (Prichard et al. 1986). In sulfide-bearing
152 dunites associated with chromitites, which form the crustal sequence overlying the mantle
153 harzburgite, PGM include Pt-, Pd-rich stibiopalladinite Pd_5Sb_2 , geversite $Pt(Sb,Bi)_2$, genkinite
154 $(Pt,Pd)_4Sb_3$, Pt-Fe-Cu alloys and Pt- and Pd-oxides. The wehrlite contains a mineral assemblage
155 formed from a more fractionated magma consisting of Pd-Cu sulfide and Pd-Pb alloys $\pm Pt$ and $\pm Au$
156 in unaltered clinopyroxenite, with Pt and Pd arsenides, antimonides and tellurides in adjacent
157 serpentinite.

158 Arsenic- and Sb-bearing PGM are only found interstitial to the chromite grains and thus are
159 associated with the serpentine rather than with melts associated with crystallisation of the chromite
160 (Prichard et al. 1994). It has been suggested that the addition of the As and Sb occurred late as the
161 ophiolite was emplaced and demonstrated by the presence of As up to 1% in serpentinites along the
162 basal thrust contact (Prichard and Lord, 1993). Thus for example the sperrylite at Cliff is a late PGM
163 formed by alteration of a primary PGM assemblage.

164 **1.5 Platinum Group Minerals at Harold's Grave**

165 Studies of the IPGE mineralogy at Harold's Grave have revealed an assemblage dominated by laurite,
166 ruthenian pentlandite (defined as pentlandite with >30 mg/g Ru), native Os and irarsite often

167 rimmed by hollingworthite. Other minerals recorded include genkinite, hongschiite, stibiopalladinite
168 and an unnamed Rh-Ni-Sb (Prichard and Tarkian, 1988).

169 There textural associations of the PGM are similar to those observed in other Shetland chromitites.
170 Euhedral Os-bearing laurite grains are included within the chromite grains, whereas Os-barren
171 laurite of irregular shape is found where the laurite is in contact with the serpentine interstitial to
172 the chromite grains. This interstitial laurite is often accompanied by native Os, irarsite and ruthenian
173 pentlandite forming composite PGM; the PPGE-bearing PGM are predominantly interstitial to the
174 chromite grains (Prichard et al. 1986; Tarkian and Prichard, 1987; Prichard et al. 1994). This PGM
175 assemblage described from the Harold's Grave chromitite was the subject of an Os-isotope study by
176 Badanina et al. (2016) with the observation that there are composite grains of laurite and Ru-Os-Ir
177 alloys within the chromite grains. These authors also observed that the PGM within the chromite
178 grains are smaller than those in interstitial positions.

179 **1.6 Osmium isotopes in the Shetland ophiolite**

180 There have been three previous studies of Os isotopes in the Shetland ophiolite. The first analysed
181 whole rock powders of chromitites resulted in $^{187}\text{Os}/^{188}\text{Os}$ values of 0.12523 for Harold's Grave,
182 0.12721 for Cliff, 0.12645 for a chromitite in the crustal dunite and 0.12790 for Quoys (Walker et al.
183 2002b). A further study on whole rock chromitites and peridotites from the ophiolite found Re-Os
184 isotope model ages of approximately 500 Ma as well as an earlier Mesoproterozoic melting event
185 (O'Driscoll et al. 2012). A third study examined Os-bearing minerals in situ in a chromitite sample
186 from Harold's Grave (Badanina et al. 2016). That study found that PGM interstitial to chromite grains
187 generally displayed a range of $^{187}\text{Os}/^{188}\text{Os}$, from 0.1235 to 0.1250, that is indistinguishable from
188 those included in chromite. They interpreted this as preservation of the ratios during alteration and
189 serpentinisation in a closed isotopic system; with PGM enclosed in chromite grains representing a
190 magmatic assemblage and interstitial PGM representing an alteration assemblage.

191 The study presented here combines in situ Os isotope measurements with the 3 dimensional
192 location of PGM, following the methodology of Godel et al. (2010, 2014), to investigate the genesis
193 and histories of each group of PGM at Harold's Grave. This approach has been further extended to
194 Os-bearing PGM from the Cliff, Quoys and Nikkavord South chromitite lenses in the mantle of the
195 Shetland ophiolite complex.

196 **2. MATERIAL AND METHODS**

197 Six micro-cores were drilled from samples of Harold's Grave chromitite and were scanned using the
198 XRADIA XRM 500 high-resolution 3D X-ray microscope system at the Australian Resources Research
199 Centre (CSIRO Mineral Resources, Kensington, Western Australia). The characteristics of the micro-

200 core, voxel sizes and number of projections used to volume reconstruction are provided in
201 supplementary Table S1. The instrument was set-up (for each sample) to maximise phase contrast
202 between chromite, Ru-pentlandite, the platinum-group minerals and silicates. For long samples
203 (HG6A and HGS), multiple tomographies were recorded along the vertical axis and stitched in 3D to
204 provide an entire view of the samples. Chromite, silicates, Ru-pentlandite and PGM were segmented
205 from the greyscale volumes using modified gradient watershed algorithm described in Godel (2013).
206 Quantitative measurements (spatial location, volume, equivalent sphere diameter referred to as ESD,
207 maximum and minimum Feret lengths, sphericity and 3D orientations of the elongation axes) were
208 calculated for each PGM. These informations were used relocate PGM during the grinding and
209 polishing processes to expose the PGM and perform their chemical and isotopic characterisation. It
210 should be noted that PGM of size smaller than the spatial resolution (Table 2) were not quantified
211 using the HRXCT.

212 The PGM were identified using a Cambridge Instruments (ZEISS NTS) S360 scanning electron
213 microscope (SEM), coupled to an Oxford Instruments INCA energy plus which included both an
214 energy dispersive (ED) and a wave dispersive (WD) X-ray analytical system at Cardiff University.
215 Chromite grains were analysed with a 20kV accelerating voltage, 20 nA beam current and fixed beam
216 size (approximately 10-15 nm) with a live-time of 50 s for ED. A cobalt standard and separate
217 chromite standard were used to monitor for instrumental drift. Many PGM (about 2,000) were
218 analysed qualitatively but a few typical common ones and the rarer ones were analysed
219 quantitatively.

220 Osmium-bearing PGM were analysed for $^{187}\text{Os}/^{188}\text{Os}$ by laser ablation MC-ICPMS, using a New Wave
221 UP 213 nm Nd:YAG laser system, coupled to a ThermoFinnigan Neptune MC-ICPMS at Durham
222 Geochemistry Centre, Durham University. Full details are given in the Appendix.

223

224

3. RESULTS

3.1 Five Generations of PGM

226 Overall five generations of PGM have been identified from the 3D volumes. These five groups consist
227 of (i) small (1-22 μm ESD) laurites often with IPGM enclosed in chromite grains, (ii) larger composite
228 PGM hosting all 6 PGE, sometimes forming clusters, located either in serpentinized zones cross
229 cutting chromite grains or on the edge outside chromite grains (referred to hereafter as interstitial
230 grains) with individual composite PGM reaching 350 μm ESD, and about 10% (in number) of grains
231 exceeding 100 μm . (iii) aligned elongate PGM (up to 100 μm in length), occurring within a few
232 chromite grains (hosting all PGE except Pd) (iv) almost spherical laurite (80 μm ESD) grains in a sheet

233 cross cutting a chromitite layer, and lastly (v) small (10 μm ESD) elongate PGM associated with
234 micro-shearing. The numbers and size range of PGM imaged in the different scans is shown in Table
235 3.

236 3.1.1 Group (i) IPGM hosted within chromite

237 Group (i) PGM are those enclosed by the chromite grains and are the smallest PGM imaged. In 3D
238 the PGM can be seen to form single equant grains or composite grains of equant and elongate PGM
239 (Fig. 2 A-F, supplementary Fig. S1). The PGM are hosted within the chromite, not associated with the
240 silicate inclusions that are also present within the chromite grains, and not associated with fractures.
241 They are evenly distributed as shown by Fig. 2 G and H.

242 Fig 2.

243 A study of HG6 showed that within the chromite grains the PGM are almost exclusively equant
244 laurite and elongate Os-Ir-Ru-Rh alloys with only two Pt-bearing PGM that form part of composite
245 PGM. These PGM are small with laurite ranging from 0.5 x 0.5 μm to 10 x 8 μm in diameter and
246 averaging 4.8 x 3.9 μm in diameter, whereas the Os-Ir-Ru-Rh alloys range from 0.5 x 0.5 to 6 x 3 μm
247 in apparent cross section diameter with an average of 3.4 x 2.2 μm . The number and area of PGM
248 exposed on a 2D slice surface of HG6 are documented according to textural position and
249 composition in Table 3 and Figs. 3 and 4. Energy-dispersive SEM analyses of the PGM are given in
250 Supplementary Table S2.

251 Fig 3

252 Fig 4

253 3.1.2 Group (ii) PGM interstitial to chromite grains

254 The PGM in this group are interstitial to chromite, usually located on the edges of the grains, and
255 occur in HG1, HG6, HG7, HG8 and HGS. Imaging in 3D appears to suggest that some large composite
256 PGM are located within a single chromite grain, but EBSD analysis of the area around one PGM
257 indicates that the surrounding chromite is in fact composed of 5 grains, and the PGM is located at
258 the junction of two grains (Fig. 5, supplementary Figs. S2, S3). This suggests that other such PGM
259 may also be located at the junctions of adjacent chromite grains, rather than being enclosed.

260 Fig 5.

261 These PGM have a very different composition to those in Group (i) (Supplementary Table S3) and are
262 much larger and more abundant. A survey of HG6 revealed the variety of PGM in this group (Fig. 3).
263 In contrast to the small laurite crystals and associated IPGM alloys enclosed in chromite belonging to
264 Group (i), interstitial PGE-bearing minerals are more varied with predominantly laurite associated
265 with native Os, irarsite and ruthenian pentlandite. Os-Ir alloys are a minor component of this

266 assemblage and the IPGM are accompanied by Pt-bearing PGM; small 1-2 μm PGMs are
267 predominant in terms of numbers of grains, but minor in terms of total volume or area (Fig. 3).

268 The interstitial IPGM and ruthenian pentlandite (Fig. 7) are accompanied by Rh-Pt-Ni- antimonides,
269 hollingworthite that rims irarsite, platarsite, Pt-Fe alloy and sperrylite. Os-poor laurite is commonly
270 rimmed by Os-rich laurite. Rare oxidised PGM have been located: one Ru-oxide and one precursor
271 Rh-Pt-Ni- antimonide. Millerite and heazlewoodite are relatively common, forming composite grains
272 with IPGM. One grain of digenite was located (Fig. 7 I) as well as one grain of chalcocite and an
273 unnamed silver copper sulfide, but Cu-bearing minerals are extremely rare. The abundance and area
274 of different PGM, both enclosed in chromite and interstitial, is shown for each sample in
275 Supplementary Figure S1.

276 The imaged part of HG6 hosts one unusually large composite PGM grain, having a maximum
277 diameter in 3D of 200 μm (Fig. 9) and shown to be 110 x 100 μm in diameter as exposed in the slice
278 in 2D. This PGM consists of laurite, ruthenian pentlandite, irarsite and native osmium.

279 Fig 6.

280 The largest group or cluster of PGM that was imaged occurs in HG7 (supplementary Fig. S3) and
281 extends over a volume of about 1 mm^3 . The PGM in this group are entirely interstitial to the
282 chromite grains. In addition to the 3D image, this was verified by the examination of textural
283 location of PGE-bearing minerals in 25 2D polished slices through the cluster (3D image and chart of
284 PGM abundances in supplementary Figs S2, S3). The PGM and ruthenian pentlandite are wrapped
285 around two chromite grains to form an 'S' shaped cluster (3D image and chart of PGM abundances in
286 supplementary Figs S2, S3). Fifteen hundred PGM were located and analysed in this cluster. They
287 include many composite PGM and all 6 PGE including most abundantly ruthenian pentlandite and
288 irarsite but also the PGE-arsenides sperrylite, hollingworthite and platarsite, as well as laurite, Pt
289 alloys and oxides, native osmium, rarer PGE antimonides and rare Pd-PGM, reflecting the low values
290 of Pd in the whole-rock PGE analyses.

291 3.1.3 Group (iii) PGM aligned within chromite grains

292 Detailed observation of the 3D morphologies of PGM reveals local clusters of large (50 μm) elongate
293 rod shaped grains with a distinct preferred orientation, enclosed within particular host chromite
294 grains (Fig. 7). EBSD analysis of a chromite containing five PGM grains with mutually parallel long
295 axes shows that the host chromite is a single crystal. PGM from this grain were analysed on sections
296 cut through these PGM, and they were found to consist of composite PGM of native Pt and native
297 Os, IrSbS (possibly tolovkite), laurite, irarsite and a Pt-Rh-Ni-antimonide representing all the PGE
298 except Pd (supplementary Fig S1).

299 Fig 7 3d aligned PGMs

300 3.1.4 Group (iv) PGM in a sheet crosscutting a chromitite layer

301 A 3D tomography image of HGS, a chromitite taken from a small 2 cm thick in situ layer, showed the
302 presence of 237 PGM within approximately 100 mm³ volume of rock, including several large (80 μm)
303 almost spherical PGM in a sheet traversing the layer at an angle of approximately 60 degrees to its
304 margins (Supplementary Fig. S4). SEM EDS analysis of these PGM within the sheet showed that they
305 are laurite with small inclusions of Os-Ir alloys, irarsite, Rh antimonide and one Ni-Fe-sulfide.

306 3.1.4 Group (v) deformed PGM

307 The Harold's Grave chromitites are folded (Brough et al. 2015) and cut by narrow shear zones. These
308 samples show some evidence of this. For example HG6A displays at least 2 stages of local narrow
309 zones of shearing. Even the PGM in these shear zones are deformed (supplementary fig s4). Such
310 shearing of PGM is observed in 2D polished thin section but in 3D the deformation is more clearly
311 observed in one case where the PGM (having probably once been a large composite PGM) are strung
312 out in a line along the shear plane. The individual PGM in this shear are also elongated in a direction
313 that is parallel to the shear-related lineation in the surrounding chromite (Fig. 15 C).

314 3.2 Os isotopes

315 Overall, initial ¹⁸⁷Os/¹⁸⁸Os data (n=90) for 2D- and 3D-imaged PGM in the Harold's Grave chromitite
316 display a range of ¹⁸⁷Os/¹⁸⁸Os from 0.118 to 0.133, with all but five being sub-chondritic. They
317 define a clear modal peak at around 0.1250, with 67 of the 90 PGM falling within uncertainty of the
318 modal range, 0.1245-0.1255 (Fig. 8; see supplementary materials Table S4 for results; correction for
319 ingrowth of ¹⁸⁷Os is never larger than 0.00009 due to very low Re/Os). This modal peak matches
320 whole-rock chromitite compositions from Harold's Grave (O'Driscoll et al., 2012; Walker et al.,
321 2002b) and corresponds to a range of Re-depletion (T_{RD}) ages from 325 to 600 Ma, with a peak at
322 ~470 Ma, based on an ordinary (O) chondrite mantle Re-Os growth curve (present day ¹⁸⁷Os/¹⁸⁸Os =
323 0.1283, ¹⁸⁷Re/¹⁸⁸Os = 0.422; Walker et al., 2002a), which is close to the formation age of the ophiolite
324 (U/Pb in zircon from a cross-cutting plagiogranite gives a minimum age of ~492 Ma; Spray and
325 Dunning, 1991). Use of a primitive mantle growth curve (Meisel et al., 2001) results in a considerably
326 older age of ~650 Ma. Most PGM belonging to groups (i) and (ii) have the same modal age close to
327 492 Ma. Four of the five Group (iii) PGM have this ¹⁸⁷Os/¹⁸⁸Os modal value, with the other having the
328 most radiogenic ratio recorded of 0.133, giving a future age.

329 Fig. 8. Os isotope data compilation

330 The main modal range of ¹⁸⁷Os/¹⁸⁸Os is similar to a previously published PGM range mainly between
331 of 0.124 and 0.125 (Badanina et al., 2016), although our modal peak is approximately 0.0005 higher

332 than that previous study. There is no clear analytical reason for this, so we suggest that it may be a
333 sampling effect, given that their range is encompassed by ours. The large range of $^{187}\text{Os}/^{188}\text{Os}$ within
334 the modal peak, and the tails to older and younger (occasionally negative) T_{RD} ages, emphasises that
335 Os model ages are most robust where large datasets are available, and individual ages in small
336 datasets carry significant uncertainty as to their meaning.

337 Lower $^{187}\text{Os}/^{188}\text{Os}$ ratios also occur, with a cluster between 0.1200 and 0.1215 ($n=4$), and several
338 others between 0.122 and 0.123 ($n=6$). Some PGM with these lower ratios occur in the same
339 polished section of chromitite as those with higher ratios; for example, two PGM from HG3 with
340 similar locations (largely surrounded, but not completely enclosed within chromite) and both
341 consisting of laurite, native Os and irarsite (probably group ii), have differing $^{187}\text{Os}/^{188}\text{Os}$ of 0.1208
342 and 0.1247. Thus, apart from their lower Os isotope ratios, these PGM are indistinguishable from
343 some PGM whose model ages correspond to the age of the ophiolite. Most PGM with lower
344 $^{187}\text{Os}/^{188}\text{Os}$ ratios of 0.120-0.122 are enclosed in chromite (Fig. 17), while all are composite grains
345 with laurite and in four cases are associated with Rh-bearing PGM (Fig. 17 A-L). One composite PGM
346 gives an even lower $^{187}\text{Os}/^{188}\text{Os}$ ratio of 0.1183 (Fig. 17 M and N). This composite PGM (consisting of
347 laurite, irarsite and native Os, partially surrounded by millerite) is unlike all the other PGM located at
348 Harold's Grave because it is located entirely enclosed in serpentine, more than 100 μm from the
349 nearest chromite grain. Almost all other interstitial PGM are either attached to the edge of a
350 chromite grain or are within $\sim 10 \mu\text{m}$.

351 There is a slight difference in the distribution of Os isotope values between enclosed and interstitial
352 PGM. A slightly lower proportion of 68% of enclosed PGM (both groups (i) and (iii), $n = 41$), fall
353 within uncertainty of the overall modal range. This compares to 75% of interstitial PGM ($n = 16$) and
354 80% ($n = 25$) of PGM that could not be definitively categorised, but are likely in many cases to have
355 been in contact with melt external to chromite.

356 Only a very limited Os isotope dataset for PGM from other Shetland chromitites is presented here.
357 Four PGM – one from Cliff and three from Quoys – gave $^{187}\text{Os}/^{188}\text{Os}$ values of 0.1270 - 0.1272 (Fig.
358 18). Using an O-chondrite evolution model, these ratios equate to Re-depletion ages between 150
359 and 175 Ma, younger (more enriched/less depleted) than those from Harold's Grave. One additional
360 PGM from Cliff, a laurite in serpentine, gave a future age ($^{187}\text{Os}/^{188}\text{Os} = 0.1300$). The less radiogenic
361 PGM from Cliff matches one bulk chromitite from that locality (Walker et al., 2002b), but a later
362 study indicates that individual chromitites, even from the same locality, may have variable
363 $^{187}\text{Os}/^{188}\text{Os}$ (0.1292; O'Driscoll et al., 2012).

364

4. DISCUSSION

365 4.1 Locations and formation of the PGM

366 Harold's Grave chromitites contain abundant PGM, and the assemblage is dominated by IPGE-
367 bearing minerals. 3D imagery allows us to determine whether the PGM are completely enclosed in
368 chromite grains or whether they have had direct contact with interstitial melt and minerals. This
369 observation is very difficult to confirm any other way. PGM observed in 2D on polished thin sections,
370 or obtained by a mineral separation technique, do not have enough textural information to allow
371 these conclusions to be reached. The PGM in Group (i) are totally enclosed by the chromite and
372 usually not associated with large silicate inclusions, with rare exceptions (Fig. 2C). Equally it is
373 possible to confirm that the PGM within the cluster identified in HG7 are completely external to the
374 chromite grains. This provides us with unambiguous spatial constraints on distinct origins of the
375 PGMs in terms of the five groups delineated above, of which Groups (i) and (ii) account for the vast
376 majority of grains imaged and analysed.

377 4.1.1. Magmatic laurite and IPGE alloys of Group (i)

378 The Group (i) PGM consist of small grains of laurite sometimes attached to Os-Ir-Ru alloys that form
379 composite PGM all totally enclosed by chromite. These PGM are ubiquitous within the chromite
380 grains. The PGM in Group (i) probably crystallised directly from the magma as the chromite grains
381 crystallised. Such PGM have been produced experimentally (Brenan and Andrews, 2001) and
382 proximity to the surface of the chromite is thought to induce IPGM formation due to a lowering of
383 oxygen fugacity in boundary layers around growing chromite crystals, thus reducing the solubility of
384 the IPGE in silicate melt (Finnigan et al. 2008). Brenan and Andrews (2001) observed that both
385 laurite and Ru-Os-Ir alloys may occur, with alloys reducing in proportion as temperature falls and as
386 sulfur fugacity increases.

387 4.1.2. Interstitial PGM clusters of Group (ii)

388 The Group (ii) PGM association largely accounts for the distinctively high IPGE contents of the
389 Harold's Grave chromitite. It is also the most challenging to explain, particularly in view of the fact
390 that the modal Os isotope compositions of groups (i) and (ii) show a high degree of similarity. PGM
391 belonging to Group (ii) are all external to the chromite grains, usually in composite grains that
392 contain more than two PGM. Sometimes they form in polymineralic clusters, this being
393 demonstrated most clearly in HG7. The assemblage is IPGM dominated along with ruthenian
394 pentlandite but also variably present are Pt-Rh-dominant PPGM, rare Pd-PPGM, minor Ni-bearing
395 PGM and very rare (only 3 grains located) Cu sulfides. Based on their larger size and distinctly
396 different chemistry, group (ii) PGM clusters are clearly not simply altered equivalents of the enclosed

397 Group (i) PGM assemblage (as inferred by Badanina et al., 2016) and they imply a distinctly different
398 petrogenesis.

399 Group (ii) PGM occur in clusters of multiple composite grains containing a small but consistent
400 proportion of sulfide minerals. This suggests an initial magmatic PGE concentration mechanism akin
401 to that proposed for the unusually PGE-enriched chromitites at Cliff: initial collection of PGE from a
402 PGE-enriched magmatic sulfide component. This at Cliff was followed by a postulated episode of
403 hydrothermal upgrading and S loss (Prichard et al., 1994). However, a simple hypothesis of sulfide
404 collection of the PGE at Harold's Grave fails on a number of grounds: very high Pt/Pd ratios due to
405 low Pd; a very low Cu content; and a sulfide assemblage dominated by Ru-rich pentlandite and a
406 complete absence of pyrrhotite or pyrite. (Unmodified Ni-bearing magmatic sulfide assemblages
407 always contain a component of Fe-sulfide as well as pentlandite, as a consequence of the restricted
408 range of metal/S ratios in magmatic sulfide liquids – Naldrett 2004). The high metal/S ratio of the
409 assemblage as a whole, as well as the absence of Cu, could potentially be explained by driving off S
410 as a mobile component in late magmatic fluids, during interaction between chromite and sulfide
411 (Naldrett et al., 1989) or during post-magmatic alteration. However, such a process fails to explain
412 the very high Pt/Pd ratio, since simple S loss would be expected to leave the residual sulfide
413 component strongly enriched in both Pt and Pd, as in the UG2 chromitites considered by Naldrett et
414 al. (2009). Hydrothermal alteration related to serpentinisation of the host ultramafic rocks is very
415 unlikely to preferentially remove Pd over Pt, on the evidence from komatiites that Pt and Pd are
416 essentially immobile in serpentinising fluids (Barnes and Liu 2012). Unlike Cliff and crustal dunite
417 chromitites, where native Cu indicates the altered remains of Cu sulfides (e.g. Prichard et al. 1994),
418 there is an absence of native Cu at Harold's Grave. Finally, any process of S loss would also have to
419 efficiently remove Re, to account for the almost complete absence of Re in the Group (ii) clusters
420 analysed (all but two PGM have Re/Os <0.0065, and all are <0.06).

421 As an alternative, we consider the possibility that the Group (ii) association may have formed by
422 direct precipitation of an assemblage of solid Os-Ir, Ru, Rh and Pt phases as a result of saturation of
423 the parent silicate melt in these phases, in the absence of sulfide. However, this model has a number
424 of major flaws. Firstly, it would require that these phases nucleated after cessation of chromite
425 growth, rather than forming a crystallisation continuum with the enclosed population of Group (i)
426 PGMs. It would require that these phases grew by a very efficient process of heterogeneous self-
427 nucleation to create the clusters, in contrast to the nucleation of the isolated laurite grains now
428 preserved within the chromite. There is no obvious reason why this change in nucleation style would
429 take place, and why it would be so particularly effective at this one locality. Furthermore, this model
430 then requires an additional ad hoc explanation for the sulfide component.

431 We therefore return to a sulfide collection model, but an additional process is required to account
432 for the observed discrepancies. This process may be PGM formation during re-dissolution of an
433 original PGE-rich cumulus magmatic sulfide component. We base this model on a combination of
434 three independently published ideas for behaviour of PGEs in magmatic sulfides: upgrading of PGE
435 within sulfide liquid by partial re-dissolution into sulfide-undersaturated magma (Kerr and Leitch,
436 2005); saturation of sulfide liquid with respect to IPGE alloys during partial melting of sulfide-bearing
437 mantle (Fonseca et al., 2012); and stabilisation of PGE alloy during desulfidation of magmatic sulfide
438 assemblages under conditions of declining sulfur fugacity (Peregoedova et al., 2004). The model of
439 Fonseca et al. (2012) is especially applicable to the problem at hand.

440 During the process proposed by Fonseca et al. (2012), the initially solid mantle sulfide assemblage
441 first melts, then progressively dissolves into the increasing volume of silicate partial melt with
442 progressive melting of the mantle silicates. As a result of the extreme partition coefficients for PGEs
443 into magmatic sulfide liquid (Mungall and Brenan 2014) the remaining sulfide liquid retains the
444 entire PGE budget of the original source composition, and consequently becomes progressively
445 enriched in PGE as the mass of sulfide drops. Close to the point at which the sulfide dissolves out
446 entirely, the PGE content of the sulfide liquid increases rapidly to the point where it becomes
447 saturated in PGM phases: Os-Ir alloys (Fonseca et al. 2012) and potentially also Pt-Fe alloy (Mungall
448 and Brenan, 2014). With higher degrees of partial melting, the remaining sulfide completely
449 dissolves into the silicate melt, which is now also constrained to be saturated in the same solid PGM
450 phases. The solid PGM phases that precipitated from the sulfide component remain behind in the
451 restite.

452 A closely analogous process may have operated within the Harold's Grave chromitites, which are of
453 course sulfide-bearing mantle rocks themselves. The PGE distribution, i.e. the presence of Pt-Pd
454 enriched as well as IPGE enriched chromitites, within the Shetland ophiolite as a whole implies that
455 the ophiolite belongs to the type formed from magmas on the cusp of sulfide saturation (Prichard et
456 al., 2008a), such that the same deposition site may have been fed over time by both sulfide-
457 saturated and sulfide-undersaturated magmas. A MORB type magma was proposed to have formed
458 the chromitite at Harold's Grave (Brough et al. 2015) and re-dissolution may have been caused by a
459 new S-undersaturated pulse of silicate magma probably of a more boninitic composition. This view is
460 supported by the presence of boninitic and MORB-like dykes intruded into the upper parts of the
461 gabbro in the Shetland ophiolite (Prichard and Lord, 1988).

462 We propose that re-dissolution of sulfide took place at Harold's Grave, giving the following
463 hypothetical sequence of events (Fig. 9).

464 **Fig. 9.**

- 465 1. Crystallisation of chromite from a magma saturated in both chromite and laurite, giving rise
466 to formation of the Group (i) assemblage; laurite grains nucleate in redox boundaries layers
467 around the growing chromite grains, as demonstrated in experimental studies by Finnigan et
468 al. (2008).
- 469 2. Deposition of sulfide liquid droplets from transiently sulfide-saturated chromitite-forming
470 liquid. These sulfides form at very high silicate/sulfide liquid mass ratios (R) giving rise to
471 very high PGE, Ni and Cu contents in the sulfide liquid. Such Ni-Cu-rich sulfide melt
472 compositions are potentially non-wetting against chromite, accounting for the dominant
473 presence of the droplets interstitial to chromite rather than enclosed within them (Brenan
474 and Rose, 2002). High R factors are the necessary consequence of co-precipitation of sulfide
475 with chromitite: owing to the low solubility of chromite in mafic magmas, the chromite itself
476 requires hundreds to thousands of times its own volume of magma to grow. The inferred
477 original sulfide abundance in the rock (and in sulfide bearing chromitites in general) is much
478 less than 1%, i.e. hundreds of times less than the chromite abundance; hence sulfides
479 achieve R values potentially as high as millions, giving rise to PGE tenors as high as percent
480 levels, calculated from the Campbell and Naldrett (1979) R-factor equation assuming initial
481 abundances of the order of 10 ppb in the silicate magma.
- 482 3. Continuing influx of sulfide-undersaturated, superheated magma through the accumulation
483 site of the chromitite causes re-dissolution of the sulfide component, further upgrading the
484 PGE content of the sulfide liquid (Kerr and Leitch 2005) and giving rise to an analogous
485 sequence of events as that proposed by Fonseca et al. (2012) for partial melting of sulfidic
486 mantle rocks. In this case, though, the sulfides are extremely PGE-enriched to begin with and
487 at or very close to saturation in solid IPGM and Pt-Fe alloy. As the PGE tenors are driven
488 upward within the diminishing volume of sulfide liquid, PGM saturation is attained and PGM
489 phases nucleate and grow within the sulfide liquid, forming clusters or composite grains (Fig.
490 9 G). The sulfide liquid component, carrying Cu, Ni, Pd and Re, eventually dissolves
491 completely back into the silicate melt, leaving behind nothing but solid PGM. Of the PGE,
492 only Pd is preferentially lost to the silicate melt owing to its inability to form solid PGM at
493 magmatic temperatures (Mungall, 2014). The relative depletion of Pt over the IPGE is
494 explained by a higher Pt solubility in silicate melt (Mungall and Brenan 2014), such that Pt
495 alloy forms very close to the sulfide disappearance point (Fig. 20G). The result is the
496 formation of the Group (ii) PGM associations, with the distinctive weakly Pt-depleted and
497 strongly Pd-depleted PGE patterns. These (clusters) subsequently undergo post-magmatic
498 alteration to form the presently preserved mineral assemblage, retaining non-radiogenic Os

499 isotopic compositions owing to efficient removal of the Re-bearing component at the
500 magmatic stage.

501 This mechanism explains many features of the Group (ii) interstitial mineral association, but still
502 leaves a problem that requires further explanation: the common presence in the Group (ii)
503 assemblages of ruthenian pentlandite. If this phase is derived from incompletely re-dissolved sulfide
504 melt, then this melt component should also have retained Pd and Re. As we have noted, the Group
505 (ii) PGM associations contain almost no Re. Four possible explanations have been considered.

- 506 1. The sulfide dissolution process takes place at a temperature within the melting range of the
507 sulfide, such that solid Ni-rich monosulfide solid solution (MSS) is stable and retained in the
508 source, while the residual Cu-rich melt is re-dissolved or physically entrained and removed,
509 as proposed by Ballhaus et al. (2006) to explain PGE fractionation during mantle melting.
510 This explanation is not favoured, as it would still involve retention of Re in the MSS
511 component, owing to the partition coefficient for Re into MSS from sulfide liquid being
512 greater than unity (Brenan, 2002). It is possible that the melt may have been Re poor owing
513 to melting during oxidizing conditions (Fonseca, pers comm. 2016) but there is no evidence
514 in the compositions of the chromite grains that the parent melts were unusually oxidised;
515 high V contents in Harold's Grave chromite (Brough et al., 2015) implies the opposite.
- 516 2. A ruthenium- and Ni-rich sulfide PGM is stabilised within the contracting sulfide droplet at a
517 higher temperature than the normal sulfide liquidus, possibly as a consequence of reaction
518 of early formed laurite with highly Ni-enriched sulfide liquid. This phase is converted to Ru-
519 pentlandite during low temperature re-equilibration and/or alteration.
- 520 3. The PGM aggregates formed by the process of complete re-dissolution of sulfide, then
521 acquired their sulfide component by subsequent reaction between IPGM and infiltrating
522 sulfide-saturated interstitial silicate melt. This process has been invoked by Barnes et al.
523 (2016) to account for an association between primary magmatic Pt-rich PGM and small
524 proportions of Ni-Cu sulfides.
- 525 4. The Ru-pentlandite is entirely a product of low-T alteration of laurite formed as part of the
526 solid PGM assemblage. This origin of Ru-pentlandite, a widespread mineral in altered
527 ophiolitic chromitites, has been proposed for example by Genkin et al. (1974). There is no
528 textural evidence for this process here, however.

529

530 None of the mechanisms proposed are entirely satisfactory and are all (particularly explanation 3)
531 somewhat ad hoc. Ru-pentlandite as a product of low-T alteration of laurite (explanation 4) is
532 preferred for simplicity, and is consistent with previous interpretations of altered PGM assemblages,

533 but lacks textural evidence, while number 2 is more coherent with the overall model but would
534 require experimental verification of the stability of a Ru-Ni-S phase at magmatic temperatures.
535 Nonetheless, the sulfide re-dissolution model explains the bulk of the critical observations, and
536 provides an intriguing link between Harold's Grave and other more general processes operating
537 within the mantle and within chromitites in general.

538 We note that the very small difference in the distribution of Os model ages between the Group (i)
539 enclosed and Group (ii) interstitial grains is consistent with a distinct derivation for the S-saturated
540 and undersaturated magma components. The slightly less radiogenic interstitial component, derived
541 from the S-undersaturated magma according to the model presented here, could have been derived
542 from a mantle source with slightly lower time-integrated sulfide content, and hence a higher Os/Re
543 ratio.

544 *4.1.3. Formation of the Group (iii) elongated aligned PGM*

545 Group (iii) PGM are distinct from the other groups in that they are entirely enclosed within chromite
546 grains and aligned approximately parallel to each other within an individual chromite grain. They are
547 considerably larger than Group (i) IPGM and they are composed of IPGM accompanied by Pt and Rh.
548 These Group (iii) PGM may have formed in two ways:

- 549 1. Those elongate aligned PGM that occur only in a few grains of chromite may have
550 crystallised along crystallographic planes of the chromite as it crystallised. One explanation
551 comes from the experimental studies by Finnigan et al. (2008) as outlined above (section
552 4.2), which demonstrated that IPGM phases nucleate preferentially in anomalously reduced
553 compositional boundary layers around growing chromite crystals. A redox gradient is
554 generated in the boundary layer owing to the preferential partitioning of ferric iron into the
555 chromite lattice; the resulting reduction of the silicate melt lowers the IPGE solubility, which
556 is a very strong positive function of fO_2 (e.g. Borisov and Palme, 1995; Brenan and Andrews,
557 2001), which itself is defined by the Fe^{3+}/Fe^{2+} ratio of the silicate melt. Finnigan et al. (2008)
558 further suggested that such boundary layers might be best developed around chromite
559 grains that were initially most chemically out of equilibrium with the host melt, such that
560 particular grains might contain multiple IPGMs while other neighbouring grains contained
561 none. This is consistent with the observations reported here for the Group (iii) PGM.
- 562 2. Alternatively, there is increasing evidence that PGE can be incorporated in solid solution
563 within chromite as it crystallises and then be ejected on cooling. This has been invoked to
564 explain IPGE-enriched chromite phenocrysts in volcanic rocks and in Bushveld marginal sills
565 (Park et al., 2012; Pagé et al. 2012; Pagé and Barnes 2013 and 2016). Experimental studies

566 suggest that the IPGE and Rh have chromite-melt partition coefficients in the range 40 to
567 200 at fO_2 around the Ni–NiO buffer (Brenan et al., 2012), and at higher fO_2 (probably
568 unrealistic for the case at hand) the values can approach 1000 (Richter et al., 2004). A recent
569 study by Barnes et al. (2016) suggests that the IPGE entered in solid solution into the
570 Stillwater chromite and then diffused into base metal sulfide inclusions forming laurite. The
571 very enriched PGE whole rock compositions of chromitites at Harold’s Grave require that
572 PGE from a large volume of magma all collected in the small volume of chromitite in this
573 particular dunite lens, the largest in the mantle harzburgite section of the Shetland ophiolite
574 (Brough et al., 2015). It is possible therefore that chromites from Harold’s Grave
575 incorporated PGE into their structure and then on cooling these exsolved to form the
576 parallel Group (iii) PGM observed in 3D. This interpretation would require that partition
577 coefficients of Ru into chromite be considerably higher than the values indicated by Brenan
578 et al. (2012), tending to favour explanation 1.

579

580 **4.2 Alteration**

581 The PGM assemblage that we observe today in these highly anomalous PGE-enriched samples from
582 Harold’s Grave is a secondary alteration assemblage; the primary assemblages having been
583 overprinted during serpentinisation of the ophiolite especially during emplacement. The basement
584 contact of the ophiolite is enriched up to 1% As (Prichard et al. 1993) swamping any magmatic As
585 signature in these rocks. The late introduction of As and Sb on ophiolite emplacement has produced
586 arsenides including sperrylite and those belonging to the irarsite, hollingworthite and platarsite solid
587 solution series, and rarer antimonides including Rh-Sb and (NiRhPt)Sb (Supplementary material
588 Table S3). Accompanying this alteration is the formation of abundant small 1-2 μm native Os grains
589 within the composite IPGM interstitial to the chromite grains. Much of this Os is likely to have been
590 derived from the alteration of Os-Ir-bearing laurite to pure RuS_2 . Subsequent weathering has
591 produced rare PGE-oxides such as the Ru-oxide observed in HG6 (Supplementary material Table S3).
592 PGE-oxides have previously been observed in the Shetland ophiolite chromitites (Prichard et al.
593 1994). The Group (iii) PGM assemblage is also likely to be an alteration assemblage with the
594 presence of PGM arsenides associated with late stage fluid influx along the sole thrust of the
595 ophiolite (Brough et al., 2015). The Pt-Rh-Ni antimonide is also a characteristic mineral formed late
596 with the introduction of antimony on ophiolite emplacement. The PGM alteration assemblages are
597 very unlikely to have been remobilized into these aligned clusters of Group (iii) and are likely
598 pseudomorphs of former PGM.

599 **4.3. Osmium isotope constraints on chromitite and PGM formation**

600 The existence of a large range of $^{187}\text{Os}/^{188}\text{Os}$ in Harold's Grave PGM, sometimes within single
601 sections (as described in results), has previously been observed in the Mayarí-Cristal ophiolite, Cuba
602 (Marchesi et al., 2011), where comparable differences in $^{187}\text{Os}/^{188}\text{Os}$ of 0.1185 to 0.1274 were found
603 in a single sample and 0.1185 to 0.1232 between two PGM only millimetres apart. As the Re/Os
604 ratios of the Harold's Grave PGM are uniformly low, variable in situ ingrowth of ^{187}Os cannot account
605 for the isotopic variations. Such variable compositions, therefore, could either represent (a)
606 inherited xenocrystic PGM; (b) pre-existing composition of the mantle through which the chromitite-
607 forming melts percolated; (c) contamination of some, but few, discrete melts by both crustal Os
608 (radiogenic) or lithospheric Os (unradiogenic); or (d) distinct mantle sources of percolating melts
609 (e.g. Marchesi et al., 2011). No experimental constraints exist for PGM transport in percolating
610 melts, but given the compositional and mineralogical similarity of PGM grains, regardless of their Os
611 isotope signature, a xenocrystic origin of isotopic heterogeneity seems highly unlikely and would
612 require extraordinary coincidence. Inheritance of the isotopic signatures from the in situ mantle also
613 seems unlikely given the small size (3 x 15 m) of the chromitite outcrop and that individual
614 potentially isotopically heterogeneous pre-existing sulfides (e.g. Harvey et al. 2006) would not
615 contain sufficient Os to account for the Os budget of an individual PGM. Contamination cannot be
616 ruled out, but is made less likely by the need for both radiogenic and unradiogenic contaminants
617 that have only affected a small proportion of PGM-forming melts. Thus, the most plausible
618 mechanism is the precipitation of isotopically heterogeneous PGM from discrete PGE-enriched melts
619 percolating through chromitite, which in some cases have distinct mantle source histories.

620 This preservation of isotopically heterogeneous PGM requires their isolation from subsequent melt
621 percolation. Gonzalez-Jimenez et al. (2012) found that interstitial PGM from the Dobromirski
622 Ultramafic Massif, Bulgaria, show greater isotopic variation than those that are enclosed, which was
623 interpreted to reflect the influence of metamorphic fluid flow. Contrary to their findings, isotopic
624 heterogeneity is rarer in the interstitial PGM in our Harold's Grave samples, perhaps due to limited
625 fluid flow. Nonetheless, it is notable that isotopic variations are present in both enclosed and
626 interstitial PGM. This implies that (i) subsequent melts do not physically come into contact with the
627 existing PGM, for example through the process of inclusion in chromitite which undoubtedly occurs
628 (e.g. Fig. 3), and/or (ii) that the PGM are chemically unaffected by contact with the melt, at least in
629 terms of exchange of osmium isotopes. Given the high Os contents of the PGM, and their stability in
630 high temperature melt systems, chemical isolation is not unexpected (e.g. see Marchesi et al., 2011).

631 **4.4. Long-term evolution of the source(s) of Shetland chromitites**

632 Of the 83 separate PGM analysed (90 analyses) from Harold's Grave, 62 have $^{187}\text{Os}/^{188}\text{Os}$ ratios that
633 fall within uncertainty of 0.1245-0.1255. Using an ordinary (O) chondrite reference model (Walker et

634 al., 2002a), the mode for the dataset (0.1250) corresponds to a Re-depletion age of ~470 Ma, which
635 is similar to the formation age of the ophiolite (~492 Ma; Spray and Dunning, 1991). The strong
636 mode within this dataset indicates that the melts that formed Harold's Grave chromitites, and the
637 PGM they contain, came predominantly from the same mantle source, or at least sources with
638 similar histories. Again assuming an O-chondrite model, this mantle was not strongly depleted or
639 enriched, having gamma Os of close to zero (a mode of ~0.1) at 492 Ma (gamma Os is the deviation
640 from the O-chondrite model in percent). If, however, the more radiogenic primitive mantle
641 evolution model is used (Meisel et al., 2001), then the modal composition would reflect a source
642 with moderate long-term depletion (sub-chondritic Re/Os) having a modal gamma Os of around -1.

643 There are several additional isotopic signatures present in Harold's Grave chromitites. The lowest
644 $^{187}\text{Os}/^{188}\text{Os}$ value recorded is 0.1183, found only in one composite interstitial PGM. This corresponds
645 to a Re-depletion age of ~1400 Ma. A larger group of PGM (n=10) also have low $^{187}\text{Os}/^{188}\text{Os}$ ratios
646 between 0.120 and 0.123, which may possibly comprise two distinct groups, one from 0.120 to
647 ~0.121 (n=4), and another between 0.122 and 0.123 (n=6). The less radiogenic of these sub-groups
648 corresponds to a Re-depletion age of 1000-1100 Ma. While it would be unwise to suggest any global
649 significance to the existence of this group, from this dataset alone, it is interesting to note that this
650 Grenvillian age has also been found in numerous larger datasets of detrital mantle-derived PGM:
651 Urals, Tasmania (Pearson et al., 2007), Dongqiao Massif, Tibet (Shi et al., 2007) and the Rhine river
652 (Dijkstra et al., 2016). In addition, some mantle peridotite datasets also contain a significant
653 proportion of this signature, including abyssal peridotites (Brandon et al., 2000; Harvey et al., 2006)
654 and Zealandia xenoliths (Liu et al., 2015; McCoy-West et al., 2013). These combined data have led to
655 the suggestion that this is a widespread (global?) mantle depletion signature (Dijkstra et al., 2016;
656 Pearson et al., 2007).

657 It has previously been noted, on a whole-rock scale, that distinct Shetland chromitite formations
658 have differing Os isotope compositions (O'Driscoll et al., 2012). Here we note that these differences
659 and also reflected in our limited data for PGM from Quoys and Cliff chromitites. The modal average
660 $^{187}\text{Os}/^{188}\text{Os}$ ratio from Harold's Grave (~0.1245-0.1255) is absent from the five Quoys and Cliff PGM
661 analysed, while the most common signature from Cliff and Quoys (~0.1272; four out of five PGM) is
662 only found in one of 90 PGM analyses from Harold's Grave (Figure 17). This modal isotope
663 composition for Cliff and Quoys reflects that those PGM have a more enriched source (or have been
664 contaminated by crustal material), than almost all from Harold's Grave (85 out of 90 PGM).

665 The variable Os isotope signatures from individual PGM from within a single chromitite, and
666 between chromitites, indicates heterogeneity of the Shetland chromitite mantle source in either
667 space, time, or both, although it is unclear over what length- and time-scale such sources would

668 exist. Given the convergent margin origin of the Shetland ophiolite, it is plausible that different
669 portions of mantle are sampled, both temporally and spatially, according to the dynamics of fluid
670 fluxing and the corresponding partial melting.

671 **5. CONCLUSIONS**

672 X-ray computed tomography has been used to identify five distinct groups of PGM in the IPGE
673 enriched chromitites from Harold's Grave in the Shetland ophiolite, of which two are predominant.
674 Group (i) PGM consist almost exclusively of laurite sometimes accompanied by IPGE alloys, entirely
675 enclosed within chromite grains. The Group (ii) PGM association occurs interstitial to chromite grains
676 with a much greater diversity of PGM than in Group (i) including laurite, native Os, irarsite-
677 hollingworthite and platarsite, sperrylite, (NiRhPtPd)Sb, PGE alloys and various PGE-oxides including
678 Ru-oxide all accompanied by ruthenian pentlandite. Group (ii) accounts for the bulk of the total
679 mass of PGMs in the samples. Group (iii) PGMs are elongate and aligned, comprise an assemblage of
680 native Pt and native Os, Pt-Os alloy, IrSbS (possibly tolovkite), laurite, irarsite and a Pt-Rh-Ni-
681 antimonide, and occur as multiple inclusions within particular individual chromite crystals only.

682 In contrast to the previous interpretation by Badanina et al. (2016), we do not regard the interstitial
683 Group (ii) aggregates as being simply altered equivalents of the Group (i) assemblage, but rather as
684 having a distinct petrogenesis. The Group (i) IPGE-rich laurites and alloys crystallised directly from
685 the silicate parent magma and were engulfed in the chromite as it grew around them. Group (ii)
686 interstitial aggregates are attributed to a two stage process involving initial collection by a sulfide
687 liquid at very high R factor, followed by re-dissolution of this sulfide liquid into a later influx of
688 sulfide-undersaturated magma. PGM containing IPGE, Pt and Rh are stabilised during the progressive
689 reduction of sulfide liquid mass, and retained in the rock after the sulfide liquid has been completely
690 re-dissolved. This process is closely akin to that postulated by Fonseca et al. (2012) to form Os-Ir
691 alloys during mantle melting.

692 The general uniformity of $^{187}\text{Os}/^{188}\text{Os}$ ratios within the sample (67 of 90 PGM fall within uncertainty
693 of 0.1245-0.1255) supports the contention of Badanina et al. (2016) that the Harold's Grave
694 chromitites have behaved as a closed system for Re and Os at outcrop scale since the time of
695 formation of the ophiolite. A small proportion of anomalously low, unradiogenic $^{187}\text{Os}/^{188}\text{Os}$ PGM
696 with one at 0.1183, and 10 between 0.120 and 0.123. These ratios are probably a consequence of
697 heterogeneities in the source of the parent magmas; specifically, long-term depleted sources. A
698 smaller proportion of anomalously radiogenic samples ($^{187}\text{Os}/^{188}\text{Os} = 0.127\text{-}0.133$; $n = 5$) attest to the
699 rarer presence of melts from more enriched mantle sources. Regardless of the source, Os isotope
700 heterogeneity is present among individual PGM, within a single hand specimen (cf. Marchesi et al.,
701 2011), requiring that PGM form from discrete melts, sometimes with distinct sources.

702 Detailed petrographic observations suggest a complicated sequence of PGM crystallisation. The
703 proposed model for the composite interstitial PGM aggregates involves a complex and probably
704 unusual sequence of events, which is reflected in the extreme rarity of chromitites like Harold's
705 Grave. However, the model of PGM formation by re-dissolution of sulfide may be a much more
706 general hypothesis with applications to PGE geochemistry in a range of magma types and settings.

707

6. ACKNOWLEDGMENTS

708 We acknowledge a Distinguished Visiting Fellowship to Prof. Hazel Prichard CSIRO that made this
709 work possible. The Os isotope analytical work in Durham was supported by a Natural Environment
710 Research Council Grant NE/F005717/1. Steve Barnes is funded by the CSIRO Science Leader scheme.
711 We thank Dr Duncan Muir for his help with the EBSD at Cardiff University We thank Dr Raul Fonseca,
712 an anonymous reviewer and Prof. Ian Campbell for their careful consideration of the manuscript.

713

8. APPENDIX – analytical methods for Os isotopes

714
715 Osmium-bearing PGM were analysed for $^{187}\text{Os}/^{188}\text{Os}$ by laser ablation MC-ICPMS, using a New Wave
716 UP 213 nm Nd:YAG laser system, coupled to a ThermoFinnigan Neptune MC-ICPMS at Durham
717 Geochemistry Centre, Durham University. All isotopes of Os were analysed, together with the key
718 elements which potentially cause isobaric interferences, ^{182}W and ^{185}Re , in the configuration: ^{182}W ,
719 ^{184}Os , ^{185}Re , ^{186}Os , ^{187}Os , ^{188}Os , ^{189}Os , ^{190}Os , ^{192}Os in L4, L3, L2, L1, C, H1, H2, H3, H4 collectors,
720 respectively. Due to the low Pt contents and relatively small size of the beams used, it was not
721 necessary to omit ^{192}Os from the analytical procedure, although we did not use this isotope for the
722 correction of mass bias, to avoid the potential effects of Pt interference on ^{192}Os . Instead, a
723 normalisation value of $^{189}\text{Os}/^{188}\text{Os} = 1.21978$ was used. Gain calibration, baselines, peak centring
724 and peak shape were all measured and checked at the start of each analytical session, with greater
725 detail given in Nowell et al. (2008a). Measurement consisted of 80 cycles each with 0.5-second
726 integration time.

727 In total, Os isotopes were analysed over 11 analytical sessions, from May 2013 to September 2014,
728 due to the need to polish down samples to expose new PGM. At the start of each session, a 1 ppm
729 DROsS osmium standard solution was analysed at least five times to assess instrumental accuracy
730 and reproducibility, and the laser ablation data were corrected for the offset of the DROsS values
731 from the accepted value ($^{187}\text{Os}/^{188}\text{Os} = 0.160924$; Nowell et al., 2008a), although the correction was
732 never more than 0.000015). Two variably doped 1 ppm DROsS solutions were also analysed to
733 determine the factors required to correct for ^{184}W , ^{186}W and ^{187}Re isobaric interferences during
734 ablation analyses. These solutions, D1 and D2, had concentrations of W at 0.05 ppm and 0.1 ppm
735 and Re at 0.01 and 0.05 ppm. Over the 11 sessions, the pure DROsS standards ($n = 54$) gave mean
736 values of $^{187}\text{Os}/^{188}\text{Os} = 0.160919 \pm 16$ (2 s.d.), $^{186}\text{Os}/^{188}\text{Os} = 0.119917 \pm 09$ and $^{184}\text{Os}/^{188}\text{Os} = 0.001297$
737 ± 14 , equating to relative reproducibilities of 98 ppm, 73 ppm and 11 ‰, respectively. Overall,
738 including the two doped solutions ($n = 21$ D1 and 15 D2) mean values were $^{187}\text{Os}/^{188}\text{Os} = 0.160920$,
739 $^{186}\text{Os}/^{188}\text{Os} = 0.119917$ and $^{184}\text{Os}/^{188}\text{Os} = 0.001298$ with relative uncertainties of 99 ppm, 74 ppm and
740 11 ‰ (when corrected to $^{189}\text{Os}/^{188}\text{Os} = 1.21978$), in excellent agreement with published data of
741 (Nowell et al., 2008a). The best fit $^{185}\text{Re}/^{187}\text{Re}$ and $^{182}\text{W}/^{186}\text{W}$, used for interference correction,
742 varied over the course of the 11 sessions by 115 ppm and 143 ppm, respectively, with average
743 values of 0.598156 and 0.929215. These variations are somewhat higher than the degree of
744 uncertainty shown by DROsS values alone, but data from each analytical session was corrected with
745 the corresponding values from that session. The additional issue that these values are determined
746 from solutions (wet plasma), and thus are not strictly identical to those of laser ablation, is
747 insignificant at the minor proportions that the interfering elements are present in the studied PGM

748 grains compared to those of the doped standards: $^{182}\text{W}/^{188}\text{Os}_{\text{Shetland PGM}}/^{182}\text{W}/^{188}\text{Os}_{\text{doped standard}}$ is
749 always <0.023 ; while $^{185}\text{Re}/^{188}\text{Os}_{\text{Shetland PGM}}/^{185}\text{Re}/^{188}\text{Os}_{\text{doped standard}}$ is <0.06 for all PGM. Most
750 importantly, the uncertainties for both the interference correction and the mean $^{187}\text{Os}/^{188}\text{Os}$ DROsS
751 value are far smaller than the range of natural variation, which is $\sim 85\%$.

752 The methods for ablation and analysis closely followed those detailed in Nowell et al. (2008b),
753 except that it was necessary to use smaller beam sizes of 12 to 30 μm , due to correspondingly small
754 grain sizes. At the smaller beam sizes, the power of the laser beam was always kept to 90-100% to
755 minimise any potential fractionation at the ablation site. Such fractionation is poorly understood
756 and is mainly a consideration for inter-element fractionation, which is of secondary importance in
757 this study because we use model age estimates rather than isochron dating methods. Nonetheless,
758 we undertook additional tests to investigate potential effects of low overall laser energy and lower
759 Os beam intensities (resulting from small laser spot sizes), compared to previous studies (Dijkstra et
760 al., 2016; Nowell et al., 2008b). Tests on the Durham University in house standard, PGM sample
761 36720 from the Urals, show that uncorrected effects on $^{187}\text{Os}/^{188}\text{Os}$ and $^{186}\text{Os}/^{188}\text{Os}$ do exist when
762 the ^{188}Os beam is less than 150 mV, due either to measurement effects or to lower overall laser
763 power – the latter as a result of small laser spot sizes of 12 μm or less, or to lower laser power of
764 $\sim 60\text{-}80\%$ on intermediate spot sizes of 20-30 μm . It has not been possible to completely deconvolve
765 instrumental and laser power effects, but an instrumental effect is more likely due to the fact that
766 $^{187}\text{Os}/^{188}\text{Os}$ (and $^{186}\text{Os}/^{188}\text{Os}$) ratios can deviate both above and below the accepted value for 36720
767 (Grain 2) of 0.12395 (measured on beam sizes of >4 V of ^{188}Os ; Nowell et al., 2008b). An error in the
768 W or Re interference correction cannot account for the variation because both elements are present
769 in similarly low proportions as in the Shetland PGM. The source of this variation, therefore, is
770 probably variation in the baseline, despite an increased baseline measurement time of 30 seconds
771 for these small beam analyses, although an unknown interference effect cannot be ruled out.

772 Regardless of the source, the tests indicate that when $^{187}\text{Os}/^{188}\text{Os}$ ratios deviate by more than
773 0.0008, then $^{184}\text{Os}/^{188}\text{Os}$ and $^{186}\text{Os}/^{188}\text{Os}$ also deviate such that these analyses are effectively filtered
774 out by the thresholds outlined below. As $^{187}\text{Os}/^{188}\text{Os}$ deviations of less than 0.0008 are not always
775 effectively screened out, the within run uncertainty on Shetland PGM analyses with ^{188}Os beams
776 <150 mV has been combined with an uncertainty of 0.00066, which is 2 s.d. on the range of offsets
777 from the true value for PGM 36720 for tests with equivalent beam sizes. A similar calculation of
778 external precision has been done for larger beam sizes, with the following uncertainties from the
779 36720 tests: 0.00045 for ^{188}Os beams of 0.15 - 0.5 V, 0.00019 between 0.5 - 1 V, and 0.00007 for >1
780 V. While the resulting uncertainties are greater than many within-run uncertainties, they remain
781 much smaller than the range observed between grains and relate to uncertainties in the Re-

782 depletion model ages ranging from 94 to 10 Ma for the range of beam sizes outlined – well within
783 the overall uncertainty on model ages due to choice of reference and much less than the difference
784 between groups of PGM identified in this study.

785 Mass bias and interfering element corrections were applied to each measurement, after which the
786 analyses were subject to a 2σ rejection. The method and corrections are discussed in greater detail
787 by Nowell et al. (2008b). The relatively high power and small grains resulted in complete destruction
788 of some PGM, in which case some cycles were omitted due to low beam sizes, below 40 mV of ^{188}Os .
789 A number of filters were applied to the overall dataset to avoid potential inaccuracies as discussed
790 above for the tests on PGM 36720. Average beam sizes below 40 mV ^{188}Os were omitted due to the
791 unreliability of ratios at this level, demonstrated for standard PGM 36720. Data were also required
792 to fall (including 1 s.e. uncertainties) within the range of 0.0011 to 0.0015 for $^{184}\text{Os}/^{188}\text{Os}$ (natural
793 ratio: ~ 0.0013) and also above 0.119500 for $^{186}\text{Os}/^{188}\text{Os}$. While this threshold value for $^{186}\text{Os}/^{188}\text{Os}$ is
794 outside the range of permissible natural values (the solar system initial is ~ 0.119825 ; modern mantle
795 is ~ 0.119835 (Brandon et al., 2000; Brandon et al., 2006)) this threshold ensures that no data
796 reported deviates from the likely true value by more than 0.00035, even at 1 s.e. uncertainties. Such
797 a deviation is insignificant compared to the natural variations observed in the $^{187}\text{Re} - ^{187}\text{Os}$ system
798 (whole $^{187}\text{Os}/^{188}\text{Os}$ range measured is 0.015, a factor of ~ 40 greater). Thus, any further filtering of
799 the data is unnecessary for meaningful $^{187}\text{Os}/^{188}\text{Os}$ comparison and has been avoided to ensure that
800 the dataset was not skewed towards large PGM, which tend to be interstitial. Uncertainties on
801 $^{184}\text{Os}/^{188}\text{Os}$ and $^{186}\text{Os}/^{188}\text{Os}$ were limited to 1 s.e. during filtering to ensure that imprecise data which
802 deviated markedly from the true values were omitted. Correction for ingrowth of ^{187}Os was
803 insignificant, because no filtered PGM had $^{187}\text{Re}/^{188}\text{Os}$ ratios greater than 0.031 (and only two of
804 whole dataset were above this), but was performed nonetheless.

805

REFERENCES

- 806 Ahmed A. H. and Arai S. (2003) Platinum-group minerals in podiform chromitites of the Oman
807 ophiolite. *Can Min* **41**, 597–616.
- 808 Arai S., Prichard H. M., Matsumoto I. and Fisher P. C. (1999) Platinum-group minerals in podiform
809 chromitite from the Kamuikotan zone, Hokkaido, northern Japan. *Res. Geol.* **49**, 39–47.
- 810 Augé T. (1986) Platinum-group mineral inclusions in chromitites from the Oman ophiolite. *Bull. de*
811 *Minéral.* **109**, 301–304.
- 812 Augé T., Legendre O. and Maurizot P. (1998) The distribution of Pt and Ru-Os-Ir minerals in the New
813 Caledonia ophiolite. In *International Platinum* (eds. N. P. Laverov and V. V. Distler). Athens,
814 Theophrastus publications. pp. 141-154.
- 815 Badanina I. Y., Malitch K. N., Lord R. A., Belousova E. A. and Meisel T. C. (2016) Closed-system
816 behaviour of the Re–Os isotope system recorded in primary and secondary platinum-group
817 mineral assemblages: Evidence from a mantle chromitite at Harold's Grave (Shetland Ophiolite
818 Complex, Scotland). *Ore Geol. Rev.* **75**, 174-185.

819 Bacuta G. C. J., Lipin B. R., Gibbs A. K. and Kay R.W. (1988) Platinum-group element abundance in
820 chromite deposits of the Acoje ophiolite block, Zambales ophiolite complex, Philippines. In
821 *Geo-Platinum Symposium Volume* (eds. H. M. Prichard, P. J. Potts, J. F. W. Bowles and S. J.
822 Cribb). Elsevier. pp. 381-382.

823 Ballhaus C., Bockrath C., Wohlgemuth-Ueberwasser C., Laurenz V. and Berndt J. (2006) Fractionation
824 of the noble metals by physical processes. *Contrib. Mineral. Petrol.* **152**, 667-684.

825 Barnes S. J. and Liu W. (2012) Pt and Pd mobility in hydrothermal fluids: evidence from komatiites
826 and from thermodynamic modelling. *Ore. Geol. Rev.* **44**, 49-58.

827 Barnes S. J., Fisher L. A., Godel B., Maier W.D., Paterson D., Howard D.L., Ryan C.G. and Laird J.S.
828 (2016) Primary cumulus platinum minerals in the Monts de Cristal Complex, Gabon: magmatic
829 microenvironments inferred from high-resolution x-ray fluorescence microscopy. *Contrib.*
830 *Mineral. Petrol.* **171**, 23-41.

831 Borisov, A. and Palme, H. (1995) Solubility of iridium in silicate melts: new data from experiments
832 with Ir₁₀Pt₉₀ alloys. *Geochim. Cosmochim. Acta* **59**, 481-485. Borisov, A. and Palme, H. (2000)
833 Solubilities of noble metals in Fe-containing silicate melts as derived from experiments in Fe-
834 free systems. *Amer. Mineral.* **85**, 1665- 1673.

835 Borisov, A. and Walker, R.J. (2000) Os solubility in silicate melts: New efforts and results. *Amer.*
836 *Mineral.* **85**, 912- 917.

837 Brandon, A.D., Snow, J.E., Walker, R.J., Morgan, J.W. and Mock, T.D. (2000) ¹⁹⁰Pt-¹⁸⁶Os and ¹⁸⁷Re-
838 ¹⁸⁷Os systematics of abyssal peridotites. *Earth and Planetary Science Letters* **177**, 319-335.

839 Brandon, A.D., Walker, R.J. and Puchtel, I.S. (2006) Platinum-Osmium Isotope Evolution of the
840 Earth's Mantle: Constraints From Chondrites and Os-Rich Alloys. *Geochimica Et Cosmochimica*
841 *Acta* **70**, 2093-2103.

842 Brenan, J.M. (2002) Re-Os fractionation in magmatic sulfide melt by monosulfide solid solution.
843 *Earth Planet. Sci Letts.* **199**, 257- 268.

844 Brenan J.M. and Andrews D. (2001) High-temperature stability of laurite and Ru–Os–Ir alloy and
845 their role in PGE fractionation in mafic magmas. *Can Mineral* **39**, 341-360.

846 Brenan, J.M, Finnigan, C.S., McDonough, W.F., Homolova, V. (2012) Experimental constraints on the
847 partitioning of Ru, Rh, Ir, Pt and Pd between chromite and silicate melt; the importance of
848 ferric iron. *Chemical Geology*, **302-303**, p.16-32

849 Brenan, J.M., McDonough, W.F. and Ash, R. (2005) An experimental study of the solubility and
850 partitioning of iridium, osmium and gold between olivine and silicate melt. *Earth Planet. Sci*
851 *Letts.* **237**, 855-872.

852 Brenan, J.M. and Rose, L.A. (2002) Experimental constraints on the wetting of chromite by sulfide
853 liquid. *Canadian Mineralogist* **40**, 1113-1126.

854 Bridges J. C., Prichard H. M., Neary C. R. and Meireles C. A. (1993) Platinum-group element
855 mineralization in the chromite-rich rocks of the Braganca massif, northern Portugal. *Trans Inst.*
856 *Min. and Metall B* **102**, 103-113.

857 Brough C. P., Prichard H. M., Neary C. R., Fisher P. C. and McDonald, I (2015) Geochemical variations
858 within podiform chromitite deposits in the Shetland Ophiolite: Implications for petrogenesis
859 and PGE concentration. *Econ. Geol.* **110**, 187–208

860 Campbell I. H. and Naldrett A. J. (1979) The influence of silicate:sulfide ratios on the geochemistry
861 of magmatic sulfides. *Econ. Geol.* **74**, 1503-1506.

862 Constantinides C. C., Kingston G. A. and Fisher P. C. (1980) The occurrence of platinum-group
863 minerals in chromitites of the Kokkinorostos chrome mine, Cyprus. In *International Ophiolite*
864 *Symposium Volume* (ed. A. Panayiotou). Geological Survey of Cyprus. pp. 93–101.

865 Corrivaux L. and Laflamme J. H. G. (1990) Minéralogie des éléments du groupe du platine dans les
866 chromitites de l'ophiolite de Thetford mines, Québec. *Can Mineral.* **28**, 579-595.

867 Derbyshire, E.J., O'Driscoll, B., Lenaz, D., Gertisser, R. and Kronz, A. (2013) Compositionally
868 heterogeneous podiform chromitite in the Shetland ophiolite complex (Scotland); implications

869 for chromitite petrogenesis and late stage alteration in the upper mantle portion of a supra-
870 subduction zone ophiolite. *Lithos* **162-163**, 279-300.

871 Dijkstra, A.H., Dale, C.W., Oberthür, T., Nowell, G.M. and Pearson, D.G. (2016) Osmium isotope
872 compositions of detrital Os-rich alloys from the Rhine River provide evidence for a global late
873 Mesoproterozoic mantle depletion event. *Earth and Planetary Science Letters* **452**, 115-122.

874 Economou-Ellopoulos M. (1996) Platinum-group element distribution in chromite ores from
875 ophiolite complexes: Implications for their exploration. *Ore Geol. Rev.* **11**, 363–381.

876 Finnigan C. S., Brenan J. M., Mungall J. E. and McDonough W. F. (2008) Experiments and models
877 bearing on the role of chromite as a collector of platinum-group minerals by local reduction. *Jl*
878 *Pet.* **49**, 1647-1665.

879 Flinn D. (1985) The Caledonides of Shetland. In *The Caledonide Orogeny - Scandinavia and related*
880 *Areas* (eds. D. G. Gee and B. A. Sturt). John Wiley and Sons Ltd. pp. 1159-1172.

881 Flinn D. and Oglethorpe J. D. (2005) A history of the Shetland Ophiolite Complex. *Scot. Jl. Geol.* **41**,
882 141-148.

883 Fonseca R. O. C., Campbell I. H., O'Neill H. S. C. and Allen C. M. (2009) Solubility of Pt in sulphide
884 mattes: Implications for the genesis of PGE-rich horizons in layered intrusions. *Geochim.*
885 *Cosmochim. Acta* **73**, 5764-5777.

886 Fonseca R. O. C., Laurenz V., Mallmann G., Luguet A., Hoehne N. and Jochum K. P. (2012) New
887 constraints on the genesis and long-term stability of Os-rich alloys in the Earth's mantle.
888 *Geochim. Cosmochim. Acta* **87**, 227-242.

889 Genkin A. D., Laputina I. P. and Mivavitskaya G. M. (1974) Ruthenium and rhodium-containing
890 pentlandite - an indicator of hydrothermal mobilization of platinum minerals. *Geol. Rudnykl*
891 *Mestarož*. **6**, 102-106 (translation 1976, *Internat. Geol. Rev.* **18**, 723-728).

892 Godel B. (2013) High-Resolution X-Ray Computed Tomography and Its Application to Ore Deposits:
893 From Data Acquisition to Quantitative Three-Dimensional Measurements with Case Studies
894 from Ni-Cu-PGE Deposits. *Econ. Geol.* **108**, 2005-2019.

895 Godel, B. M., Barnes, S. J., Barnes, S.-J., Maier, W. D. (2010). Platinum ore in 3D: Insights from high-
896 resolution X-ray computed tomography. *Geology* **38**, 1127-1130.

897 Godel, B., Rudashevsky, N. S., Nielsen, T. F. D., Barnes, S. J., Rudashevsky, V. N. (2014). New
898 constraints on the origin of the Skaergaard Intrusion Cu-Pd-Au mineralization: Insights from
899 high-resolution X-ray computed tomography. *Lithos* **190-191**, 27-36.

900 González-Jiménez J. M., Griffin W. L., Proenza A., Gervilla F., O'Reilly S. Y., Akbulut M., Pearson N. J.
901 and Arai S. (2014) Chromitites in ophiolites: How, where, when, why? Part II. The
902 crystallisation of chromitites. *Lithos* **190-191**, 140-158.

903 Griffin W. L., Spetsius Z. V., Pearson N. J., and O'Reilly S. Y. (2002) *In situ* Re-Os analysis of sulfide
904 inclusions in kimberlitic olivine: New constraints on depletion events in the Siberian
905 lithospheric mantle. *Geochem. Geophys. Geosystems* **3**, 1-25.

906 Harvey, J., Gannoun, A., Burton, K.W., Rogers, N.W., Alard, O. and Parkinson, I.J. (2006) Ancient melt
907 extraction from the oceanic upper mantle revealed by Re-Os isotopes in abyssal peridotites
908 from the Mid-Atlantic ridge. *Earth and Planetary Science Letters* **244**, 606-621.

909 Kerr A. and Leitch A. M. (2005) Self-Destructive Sulfide Segregation Systems and the Formation of
910 High-Grade Magmatic Ore Deposits. *Econ. Geol.* **100**, 311-332.

911 Kozul H., Prichard H. M., Melcher F., Fisher P. C., Brough C. and Stueben D. (2014) Platinum group
912 element (PGE) mineralisation and chromite geochemistry in the Berit ophiolite
913 (Elbistan/Kahramanmaraş), SE Turkey. *Ore Geol. Rev.* **60**, 97–111.

914 Liu J., Scott J. M., Martin C. E. and Pearson D. G. (2015). The longevity of Archean mantle residues in
915 the convecting upper mantle and their role in young continent formation. *Earth. Planet. Sci.*
916 *Lett.* **424**, 109-118.

917 Ludwig, K.R. (2003) User's manual for Isoplot 3.00: a geochronological toolkit for Microsoft Excel.
918 Kenneth R. Ludwig.

919 Marchesi, C., Gonzalez-Jimenez, J.M., Gervilla, F., Garrido, C.J., Griffin, W.L., O'Reilly, S.Y., Proenza,
920 J.A. and Pearson, N.J. (2011) In situ Re-Os isotopic analysis of platinum-group minerals from
921 the Mayari-Cristal ophiolitic massif (Mayari-Baracoa Ophiolitic Belt, eastern Cuba):
922 implications for the origin of Os-isotope heterogeneities in podiform chromitites. *Contrib.*
923 *Mineral. Petrol.* **161**, 977-990.

924 McCoy-West, A.J., Bennett, V.C., Puchtel, I.S. and Walker, R.J. (2013) Extreme persistence of cratonic
925 lithosphere in the southwest Pacific: Paleoproterozoic Os isotopic signatures in Zealandia.
926 *Geology* **41**, 231-234.

927 Meisel, T., Walker, R.J., Irving, A.J. and Lorand, J.P. (2001) Osmium isotopic compositions of mantle
928 xenoliths: A global perspective. *Geochimica et Cosmochimica Acta* **65**, 1311-1323.

929 Mungall, J.E. (2014) Geochemistry of Magmatic Ore Deposits, in: Holland, H.D., Turekian, K.K. (Eds.),
930 *Treatise on Geochemistry (Second Edition)*. Elsevier, Oxford, pp. 195-218.

931 Mungall J. E. and Brenan, J. M. (2014) Partitioning of the platinum-group elements and Au between
932 sulfide liquid and basalt and the origins of mantle-crust fractionation of the chalcophile
933 elements: *Geochim. Cosmochim. Acta* **125**, 265-289.

934 Naldrett A. J. (2004) *Magmatic Sulfide Deposits: Geology, Geochemistry and Exploration*. Springer,
935 Heidelberg.

936 Naldrett, A.J., Lehmann, J. and Auge, T. (1989) Spinel non-stoichiometry and reactions between
937 chromite and closely associated sulphides, with examples from ophiolite complexes, in:
938 Prendergast, M.D., Jones, M.J. (Eds.), *Magmatic sulphides - Zimbabwe Volume*. Inst. Min. and
939 Metall., London, pp. 221-228.

940 Naldrett, A.J., Kinnaird, J.A., Wilson, A., Yudovskaya, M.A., McQuade, S., Chunnett, G., and Stanley,
941 C., 2009, Chromite composition and PGE content of Bushveld chromitites: Part 1 - the Lower
942 and Middle Groups: *Transactions of the Institute Mining and Metallurgy, B*, v. 118, p. 131-161.

943 Nowell, G.M., Luguët, A., Pearson, D.G. and Horstwood, M.S.A. (2008a) Precise and accurate
944 ¹⁸⁶Os/¹⁸⁸Os and ¹⁸⁷Os/¹⁸⁸Os measurements by multi-collector plasma ionisation mass
945 spectrometry (MC-ICP-MS) part I: Solution analyses. *Chemical Geology* **248**, 363-393.

946 Nowell, G.M., Pearson, D.G., Parman, S.W., Luguët, A. and Hanski, E. (2008b) Precise and accurate
947 ¹⁸⁶Os/¹⁸⁸Os and ¹⁸⁷Os/¹⁸⁸Os measurements by Multi-collector Plasma Ionisation Mass
948 Spectrometry, part II: Laser ablation and its application to single-grain Pt-Os and Re-Os
949 geochronology. *Chemical Geology* **248**, 394-426.

950 O'Driscoll B., Day J. M. D., Walker R. J., Daly J. S., McDonough W. F. and Piccoli P. M. (2012) Chemical
951 heterogeneity in the upper mantle recorded by peridotites and chromitites from the Shetland
952 Ophiolite Complex, Scotland. *Earth. Planet. Sci. Lett.* **333-334**, 226-237.

953 Ohnenstetter M., Johan Z., Coherie A., Fouillac A., Guerrot C., Ohnenstetter D., Chaussidon M.,
954 Rouer O., Makovicky E., Makovicky M., Rose-Hansen J., Karup-Moller S., Vaughan D., Tumer
955 G., Patrrick R. A. D., Gize A.P., Lyon I. and McDonald I. (1999) New exploration methods for
956 platinum and rhodium deposits poor in base-metal sulfides. *Trans Inst. Min. Metall. B*, **108**,
957 119-150.

958 Orberger B., Fredrich G. and Woermann E. (1988) Platinum-group element mineralisation in the
959 ultramafic sequence of the Acoje ophiolite block, Zambales, Philippines. In *Geo-Platinum*
960 *Symposium Volume* (eds. H. M. Prichard, P. J. Potts, J. F. W. Bowles and S. J. Cribb). Elsevier. pp.
961 361-380.

962 Page N. J. and Talkington R W. (1984) Palladium, platinum, rhodium, ruthenium, and iridium in
963 peridotites and chromitites from ophiolite complexes in Newfoundland. *Can. Mineral.* **22**,
964 137-149.

965 Page N., Cassard D. and Haffty J. (1982) Palladium, platinum, rhodium, ruthenium, and iridium in
966 chromitites from the Massif du Sud and Tiebaghi Massif, New Caledonia. *Econ. Geol.* **77**, 1571-
967 1577.

- 968 Pagé P and Barnes S-J. (2013) Improved in-situ determination of PGE concentration of chromite by
 969 LA-ICP-MS: Towards a better understanding. *Mineral Deposit research for a high tech world,*
 970 *12th Biennial SGA Meeting, Uppsala. #1050-1053 (abstr.).*
- 971 Pagé P. and Barnes S-J. (2016) The influence of chromite on osmium, iridium, ruthenium and
 972 rhodium distribution during early magmatic processes. *Chem. Geol.* **420**, 51-68.
- 973 Pagé, P., Barnes, S.-J., Bedard, J.H. and Zientek, M.L. (2012) In situ determination of Os, Ir, and Ru in
 974 chromites formed from komatiite, tholeiite and boninite magmas; implications for chromite
 975 control of Os, Ir and Ru during partial melting and crystal fractionation. *Chem. Geol.* **302-303**,
 976 3-15.
- 977 Park J-W., Campbell I. H. and Eggins S. M. (2012) Enrichment of Rh, Ru, Ir and Os in Cr spinels from
 978 oxidized magmas: evidence from the Ambae volcano, Vanuatu. *Geochim Cosmochim Acta* **78**,
 979 28-50.
- 980 Pearson, D.G., Parman, S.W. and Nowell, G.M. (2007) A link between large mantle melting events
 981 and continent growth seen in osmium isotopes. *Nature* **449**, 202-205.
- 982 Pearson N. J., Alard O., Griffin W. L., Jackson S. E., and O'Reilly S. Y. (2002) *In situ* measurement of
 983 Re-Os isotopes in mantle sulfides by laser ablation multicollector-inductively coupled plasma
 984 mass spectrometry: analytical methods and preliminary results. *Geochim Cosmochim. Acta* **66**,
 985 1037-1050.
- 986 Pedersen R.B., Johannesen G.M. and Boyd, R. (1993) Stratiform PGE mineralisations in the ultramafic
 987 cumulates of the Leka ophiolite complex, central Norway. *Econ. Geol.* **88**, 782-803.
- 988 Peregoedova, A., Barnes, S. J., and Baker, D. R., 2004, The Formation of Pt-Ir Alloys and Cu-Pd-Rich
 989 Sulfide Melts by Partial Desulfurization of Fe-Ni-Cu Sulfides: Results of Experiments and
 990 Implications for Natural Systems: *Chemical Geology*, v. 208, p. 247-264.
- 991 Prichard H. M. (1985) The Shetland Ophiolite, In *The Caledonide Orogeny - Scandinavia and related*
 992 *Areas* (eds. D. G. Gee and B. A. Sturt). John Wiley and Sons Ltd. pp. 1173-1184.
- 993 Prichard H. M. and Brough, C.P. (2009) Potential of ophiolite complexes to host PGE deposits. In *New*
 994 *Developments in magmatic Ni-Cu and PGE deposits* (eds. C. Li and E. M. Ripley). Beijing,
 995 Geological Publishing House. pp. 277 - 290.
- 996 Prichard H. M. and Lord, R.A. (1988) The Shetland ophiolite: Evidence for a supra-subduction origin
 997 and implications for PGE mineralization. In *Mineral Deposits in the European Community* (eds.
 998 J. Boissonnas and P. Omenetto). Springer Verlag. pp. 289-302.
- 999 _____ (1990) Platinum and palladium in the Troodos ophiolite complex, Cyprus. *Can. Mineral.* **28**,
 1000 607-617.
- 1001 _____ (1993) An overview of the PGE concentrations in the Shetland ophiolite complex. In
 1002 *Magmatic Processes and Plate Tectonics* (eds. H. M. Prichard, T. Alabaster, N. B. Harris and C.
 1003 R. Neary). Volume 76, Geological Society of London. p p. 273-294.
- 1004 Prichard H. M., and Tarkian M. (1988) Platinum and palladium minerals from two PGE-rich localities
 1005 in the Shetland Ophiolite Complex. *Can. Mineral.* **26**, 979-990.
- 1006 Prichard, H.M., Barnes, S.J. and Godel, B., 2017. A mechanism for chromite growth in ophiolite
 1007 complexes: Evidence from 3d high-resolution x-ray computed tomography images of chromite
 1008 grains in Harold's Grave chromitite in the Shetland ophiolite. *Mineralogical Magazine*,
 1009 accepted.
- 1010 Prichard H. M., Economou-Eliopoulos M. and Fisher P. C. (2008b) Platinum-group minerals in
 1011 podiform chromitite in the Pindos ophiolite complex, Greece. *Can. Mineral.* **46**, 329 - 341.
- 1012 Prichard H. M., Ixer R. A., Lord R. A., Maynard J. and Williams N. (1994) Assemblages of platinum-
 1013 group minerals and sulfides in silicate lithologies and chromite-rich rocks within the Shetland
 1014 Ophiolite. *Can. Mineral.* **32**, 271-294.
- 1015 Prichard, H.M., Lord, R.A. and Neary, C.R. (1996) A model to explain the occurrence of platinum- and
 1016 palladium-rich ophiolite complexes. *J. Geol. Soc. London* **153**, Part 2, 323-328.

1017 Prichard H. M., Neary C. R., Fisher P. C. and O'Hara M. J. (2008a) PGE-rich podiform chromitites in
1018 the Al'Ays Ophiolite complex, Saudi Arabia: An example of critical mantle melting to extract
1019 and concentrate PGE. *Econ. Geol.* **103**, 1507-1529.

1020 Prichard H. M., Neary C. R. and Potts P.J. (1986) Platinum-group minerals in the Shetland
1021 Ophiolite. In *Metallogeny of the Basic and Ultrabasic Rocks* (eds. M. J. Gallagher, R. A.
1022 Ixer, C. R. Neary and H. M. Prichard). *Inst. Min. Metall.* pp. 395-414.

1023 Righter, K., Campbell, A.J., Humayun, M. and Hervig, R.L. (2004) Partitioning of Ru, Rh, Pd, Re,
1024 Ir and Au between Cr-bearing spinel, olivine, pyroxene and silicate melts. *Geochimica et*
1025 *Cosmochimica Acta* **68**, 867-880.

1026 Shi, R.D., Alard, O., Zhi, X.C., O'Reilly, S.Y., Pearson, N.J., Griffin, W.L., Zhang, M. and Chen,
1027 X.M. (2007) Multiple events in the Neo-Tethyan oceanic upper mantle: Evidence from
1028 Ru-Os-Ir alloys in the Luobusa and Dongqiao ophiolitic podiform chromitites, Tibet.
1029 *Earth and Planetary Science Letters* **261**, 33-48.

1030 Shirey S. B. and Walker R. J. (1998) The Re-Os isotope system in cosmochemistry and high-
1031 temperature geochemistry. *An. Rev. Earth. Planet. Sci.* **26**, 423-500.

1032 Silverman, B.W. (1986) *Density estimation for statistics and data analysis*. CRC press.

1033 Spray, J.G., Dunning, G.R., 1991. A U/Pb age for the Shetland Islands oceanic fragment, Scottish
1034 Caledonides: evidence from anatectic plagiogranites in 'layer 3' shear zones. *Geological*
1035 *Magazine* **128**, 667-671.

1036 Tarkian M. and Prichard H. M. (1987) Irarsite-Hollingworthite Solid-Solution Series and Other
1037 Associated Ru-, Os-, Ir-, and Rh bearing PGM's from the Shetland Ophiolite Complex. *Min. Dep.*
1038 **22**, 178-184.

1039 Walker, R.J., Horan, M.F., Morgan, J.W., Becker, H., Grossman, J.N. and Rubin, A.E. (2002a)
1040 Comparative Re-187-Os-187 systematics of chondrites: Implications regarding early solar
1041 system processes. *Geochimica et Cosmochimica Acta* **66**, 4187-4201.

1042 Walker, R.J., Prichard, H.M., Ishiwatari, A. and Pimentel, M. (2002b) The osmium isotopic
1043 composition of convecting upper mantle deduced from ophiolite chromites. *Geochimica et*
1044 *Cosmochimica Acta* **66**, 329-345.

1045 Xiong, y. Hydrothermal transport and deposition of Rhenium under subcritical conditions revisited.
1046 *Economic Geology* **101**, 471-478.

1047 Zhou M-F., Robinson P.T., Malpas J. and Li Z. (1996) Podiform Chromitites in the Luobusa Ophiolite
1048 (Southern Tibet): Implications for Melt-Rock Interaction and Chromite Segregation in the
1049 Upper Mantle. *Jl Pet.* **37**, 3-21.

1050

1051 Figure Captions

1052 Figure 1. Map of the Shetland ophiolite (diagram adapted from Brough et al. 2014).

1053 Figure 2. A) to F) 3D computed tomography images of PGM in sample HG6 (PGM in blue) and sample
1054 HG6A (PGM in red) showing individual laurite (round) and composite laurite and IPGE alloys
1055 (elongate and angular). A) and B) are composite grains, C) shows a laurite attached to a silicate
1056 inclusion (black) in the chromite which is not in contact with any external silicate, E) and F) are
1057 laurites not associated with elongate Os-Ir alloys. The images show that the individual PGM and the
1058 one PGM attached to a silicate inclusion are entirely enclosed in chromite; an observation that can
1059 only be confirmed in a 3D image. G) PGM in HG6A shown within the two 3D computed tomography
1060 partially imaged chromite grains (outlined in black and separated by serpentine in pale green), and
1061 H) a close up of part of one of these grains shown by a box on G) revealing that the locations of PGM
1062 (red and circled in red) are approximately evenly distributed and predominantly located away from
1063 silicate equant shaped silicate inclusions (dark grey and blue) and silicate filled fractures (blue) that
1064 cross the chromite grain.

1065 Figure 3. Abundance of types of PGM enclosed in the chromite grains belonging to Group (i)
1066 (enclosed in chromite grains – A and B) and Group (ii) PGE-bearing minerals interstitial to the
1067 chromite grains in HG6 (C and D), A and C) classification by numbers of PGM grains observed and B
1068 and D) by sectional area.

1069 Figure 4. Back scattered scanning electron microscope images of polished thin sections of typical
1070 examples of laurites (Lrt) and associated PGM alloys and silicate inclusions (dark grey or black)
1071 located within chromite grains in HG6. B) and G) are composite grains of laurite, Os-Ir-Ru alloy and
1072 very small Pt-bearing PGM.

1073 Fig. 5 A-C. Group (ii) PGM are defined as those located interstitial to the chromite grains. Some large
1074 composite PGM appear to be enclosed in chromite grains but EBSD reveals that the chromite grains
1075 are often divided into groups of grains. A) A composite PGM belonging to group (ii) that appears to
1076 be enclosed in a chromite grain shown in B). The PGM is marked by a white circle. C) EBSD image of
1077 the chromite grain containing the PGM. The area of the EBSD analysis is marked by a white rectangle
1078 shown in B). The EBSD image shows that the chromite grain is composed of several chromite grains,
1079 with different orientations indicated by different colours, and the PGM cluster is at the junction of
1080 two of these grains. D-I, Typical examples of PGM located interstitial to chromite grains in HG6
1081 observed as a back scattered SEM image in polished thin section. D) composite grain of laurite,
1082 enclosing grains of irarsite and many smaller grains of native Os, E) laurite rimmed by Os-rich laurite, F)
1083 a composite grain of laurite rimmed by Os-rich laurite containing abundant small grains of native Os,

1084 all attached to irarsite rimmed by hollingworthite and a Pt-Fe alloy, and associated with a Ru-oxide
1085 that is located adjacent to the laurite, G) sperrylite (PtAs₂), H) a Rh-Ni-Pt-antimonide and
1086 sulpharsenides associated with heazlewoodite and digenite and I) composite grain of laurite with
1087 irarsite and heazlewoodite enclosing native Os.

1088 Figure 6. Computed tomography 3D image of HG6 showing a circular slice of chromitite with
1089 chromite grains shown in grey, silicate in black and PGM in blue. A) view looking at the image
1090 oriented with the long axis of the sample core at right angles to the plane of view and B) view at
1091 right angles to A). The large PGM is shown in Figure 10. C) view of the entire largest PGM grain and
1092 associated smaller grains of ruthenian pentlandite and Pt-Rh-Sb, (all white) interstitial to chromite
1093 grains (grey) and surrounded by silicate (black), D) Close up of the large grain showing that it is a
1094 composite grain of ruthenian pentlandite, laurite, irarsite and many tiny grains of native Os, E) close
1095 up of area outlined by a box in D) showing irarsite labelled 1 and 2 with 2 containing more Rh and 3
1096 hollingworthite (analyses at locations 1-3 given in Table 5) surrounded by laurite and ruthenian
1097 pentlandite both hosting native Os. Abbreviations used:- Lrt - laurite, (Ru-Pn) = ruthenian
1098 pentlandite, Os = native Osmium.

1099 Figure 7. 3D computed tomography image of HG1 showing PGM (red) above a view of a circular
1100 basal slice through the core of chromitite with chromite (black) and interstitial silicate (blue). A) all of
1101 the PGM imaged in red. B) close-up of the aligned PGM ringed in A) and coloured blue in Figure 13.
1102 They occur in one chromite grain shown below the PGM with the lowest PGM just visible above the
1103 grain.

1104 Fig 8. Osmium isotope frequency plots – distribution of ¹⁸⁷Os/¹⁸⁸Os and corresponding Re depletion
1105 (T_{RD}) ages in Os-rich mono-mineralic or composite PGM grains from Harold's Grave. A, all
1106 measurements; B, grains entirely enclosed in chromite; C, grains or clusters within interstitial silicate,
1107 or with indeterminate relationships to chromite. Any duplicate analyses were excluded (hence 83
1108 analyses in total). The curves were calculated using Isoplot (Ludwig, 2003). A uniform 'bandwidth'
1109 uncertainty of 0.0005 was used, which is slightly larger than the optimal bandwidths (0.0003 to
1110 0.0004) according to Silverman's rule of thumb (Silverman, 1986). The increased bandwidth was
1111 used to limit exaggeration of peaks produced by small numbers of isotopically distinct grains. The
1112 histograms provide an alternative representation.

1113 Figure 9. Model of PGM formation, A) laurite and Os-Ir-Ru alloys crystallise as the chromite
1114 crystallises, group (i), group (iii) also crystallise in a few chromite grains, B) remaining PGE are
1115 collected by immiscible sulphide droplets that collect interstitially to the chromite grains with
1116 silicates, C) sulfides dissolve into a passing PGE-undersaturated silicate magma while laurite

1117 continues to crystallise, D) further S loss to the silicate magma results in Os-Ir alloys forming, E)
1118 further S loss allows Pt PGM to form close to the point of final dissolution of sulfide, while some
1119 laurite reacts with the sulfide liquid to form Ru-pentlandite as Pd and Cu dissolve into the silicate
1120 magma as all remaining sulfide liquid dissolves, F) PGM alter as As is introduced on emplacement of
1121 the ophiolite; local shearing of chromite deforms PGM, G). Evolution of PGE contents of sulfide melt,
1122 assuming initial formation from a boninite-like parent magma at high R value, followed by
1123 progressive increase of PGE tenor as sulfide dissolves, to the point of saturation in Os-Ir phases after
1124 ~50% dissolution, and Pt PGM phase(s) close to final sulfide disappearance point.

1125

1126 Electronic supplementary material

1127 Figures/images:

1128 Figure S1 was 8 Abundance of PGM enclosed in chromite or interstitial to the chromite and for HG1
1129 abundance of elongate and oriented PGM enclosed in chromite. A) number of PGM in HG6, B) area
1130 of PGM in HG6, C) number of PGM in HG1 and HG 8, D) area of PGM in HG 1 and 8 and E) areas of
1131 PGM in the interstitial cluster in HG 7.

1132 Figure S2 was 10. 3D computed tomography images of a cluster of PGM present in HG7, A) image
1133 showing the distribution of PGM in the whole of the core imaged, B) close up of the cluster or group
1134 of PGM located in HG7 showing the PGM (red) and the ruthenian pentlandite (pale green) with a
1135 slice of chromitite below and in the background showing chromite grains (light grey) and interstitial
1136 silicate (dark grey) and C) rotated image of the same cluster shown in B) revealing how the PGM
1137 form an 'S' shape caused by the PGM being wrapped around two chromite grains (whose edges are
1138 outlined in white) . Vertical height of cluster = approx. 0.9 mm.

1139 Figure S3 was 11. Relative abundance/area of IPGE-bearing minerals in the cluster of PGM in HG7 A)
1140 plotted by area of IPGE-bearing minerals observed and B) also by area with the exclusion of the two
1141 most abundant PGE-bearing minerals which are ruthenian pentlandite and irarsite (Shown in A).

1142 Fig. S4 was 14. PGM located in a co-planar array that traverses a layer of chromitite probably filling
1143 an annealed fracture. A, B) Perspective view of a 3D tomography image of a microcore showing
1144 PGM. A), chromite in blue, silicates in red. B) same volume, with PGM shown in red. Note coplanar
1145 array, ringed, C, perspective view showing orthogonal planes through the image (chromite darker
1146 grey, silicate lighter) with one of these planes arranged parallel o the planar array of PGMs. D) and E)
1147 are large laurites forming part of the planar array.

1148 Figure S5 was 15. 3D computed tomography image of chromitite in sample HG6A showing two
 1149 phases of shearing of the PGM within narrow shear zones cross cutting the sample. A) section of
 1150 HG6A showing a grain of chromite with serpentine filled undeformed pull-apart textures (p, two sub-
 1151 vertical features centre and far right, shown in blue and black), silicate inclusions (i, shown as equant
 1152 dark areas) and a cross cutting shear (s, picked out by parallel rows of dark dots crossing the entire
 1153 area from bottom right to top left). D (deformed) and E (undeformed) PGM in the shear zone and
 1154 away from the shear zone respectively (red). B) another area of sheared PGM (red) shown as two
 1155 clusters (1 and 2) in the shear zone which is marked by a line of serpentine S that is picked out in
 1156 dark grey as it crosses the chromite grain (light grey) shown in a computed tomography imaged slice
 1157 below the PGM. The larger cluster forms a row of PGM that have been broken up and aligned within
 1158 the plane of the shear. C) Close up of the larger cluster of PGM (1) showing that it has been sheared
 1159 into a line and then sheared again deforming individual PGM in a second direction (shown as sub-
 1160 horizontal). Shear directions indicated by black arrows. D) sheared PGM, E) unsheared PGM that is
 1161 not in the shear zone and F) photomicrograph of a sheared PGM as viewed in 2D in a polished block
 1162 in sample Q3 from Harold's Grave.

1163

1164 Fig. S6 was 17. Composite Os-bearing PGM, that have low $^{187}\text{Os}/^{188}\text{Os}$ ratios, all from Harold's Grave.
 1165 Pairs of back scattered scanning electron microscope photomicrographs showing details of the
 1166 composite PGM at high magnification and textural sites of the PGM in chromite at low
 1167 magnification, Lrt = laurite, Ru-pn = ruthenian pentlandite, Chr = chromite and Si = altered silicate,
 1168 mainly serpentine but with some Cr-chlorite, A) to L) have ages that correspond to ~1150 Ma and M)
 1169 and N) have an age corresponding to ~1400 Ma. Os isotope data as follows: A) and B) HG3
 1170 $^{187}\text{Os}/^{188}\text{Os}$ 0.1208; C) and D) HG5 $^{187}\text{Os}/^{188}\text{Os}$ 0.12191; E) and F) HG10 $^{187}\text{Os}/^{188}\text{Os}$ 0.1205; G) and H)
 1171 HG4 $^{187}\text{Os}/^{188}\text{Os}$ 0.1220; I) and J) HG1 $^{187}\text{Os}/^{188}\text{Os}$ 0.1211; K) and L) HG7 $^{187}\text{Os}/^{188}\text{Os}$ 0.1211; M) and N)
 1172 HG4 $^{187}\text{Os}/^{188}\text{Os}$ 0.1183.

1173 Fig. S7 was 18. Composite Os-bearing PGM, from podiform chromitite in the mantle harzburgite in
 1174 other sites than Harold's Grave, A) and B), Cliff C)-F) and Quoys G)-L). Pairs of back scattered
 1175 scanning electron microscope photomicrographs showing details of the composite PGM at high
 1176 magnification and textural sites of the PGM in chromite at low magnification, Lrt = laurite, Ru-pn =
 1177 ruthenian pentlandite, Chr = chromite and Si = altered silicate, mainly serpentine but with some Cr-
 1178 chlorite, ages correspond to those of the ophiolite or slightly younger. Os isotope data as follows:
 1179 A)and B) Nikkavord South $^{187}\text{Os}/^{188}\text{Os}$ of ~0.1266 (but data rejected due to low $^{186}\text{Os}/^{188}\text{Os}$ ratio),
 1180 C)and D) Cliff $^{187}\text{Os}/^{188}\text{Os}$ 0.1300, E)and F) Cliff $^{187}\text{Os}/^{188}\text{Os}$ 0.12721, G)and H) Quoys $^{187}\text{Os}/^{188}\text{Os}$ s
 1181 0.12708, I)and J) Quoys $^{187}\text{Os}/^{188}\text{Os}$ 0.12723, K)and L) Quoys $^{187}\text{Os}/^{188}\text{Os}$ 0.12720.

1182

SUPPLEMENTARY MATERIAL – Data Tables

1183

1184 Table S1 – size and spatial resolution data on samples analysed by HRXCT

1185 Table S2 - Semi-quantitative SEM analyses of laurite and IPGE alloys enclosed within chromite grains.

1186 Table S3 - Quantitative analyses of PGM external to chromite grains

1187 Table S4 - Table of complete Os isotope data (Excel file)

1188

1189

1190

1191

Table 1. PGE analyses of chromitites examined in this study (From Brough et al. 2014).

Sample Number	Pt	Pd	Rh	Os	Ir	Ru	Total PGE
	ppb	ppb	ppb	ppb	ppb	ppb	ppb
HG1	474	40	349	1647	2040	3400	7950
HG6	566	40	422	2968	2861	7311	14168
HG7	785	69	397	1324	2270	3483	8328
HG8	685	36	344	1479	2088	3183	7815

Table 2. PGM imaged in the 5 samples analysed in 3D. HG8 is less massive chromitite than the other samples.

Sample No.	No. Of PGM imaged	Largest PGM Microns Length	PGM Width	Smallest PGM Microns Length	PGM Width
HG6A	51	22	15	1.4	0.7
HG6	17	199	121	3.4	3.4
HG1	74	293	224	19.8	19.8
HG7	46	644	220	19.8	14.0
HG8	7	222	158	19.8	19.8

Table 3 Numbers and areas of PGM analysed in HG6 separated into interstitial and enclosed by chromite

	Interstitial		Enclosed	
	No. PGM	Area PGM	No. PGM	Area PGM
Laurite	17	10580	9	221
IrAsS	35	1231		
Ru pent	13	1182		
Native Os	115	490		
(NiRhPt)Sb	7	52		
RhIrAsS	3	43		
PtFe	3	42	1	0.25
RuO	1	32		
PtAs	2	24		
OsIr alloy	5	6	6	53
PtIrAs	2	1		

Figure 1

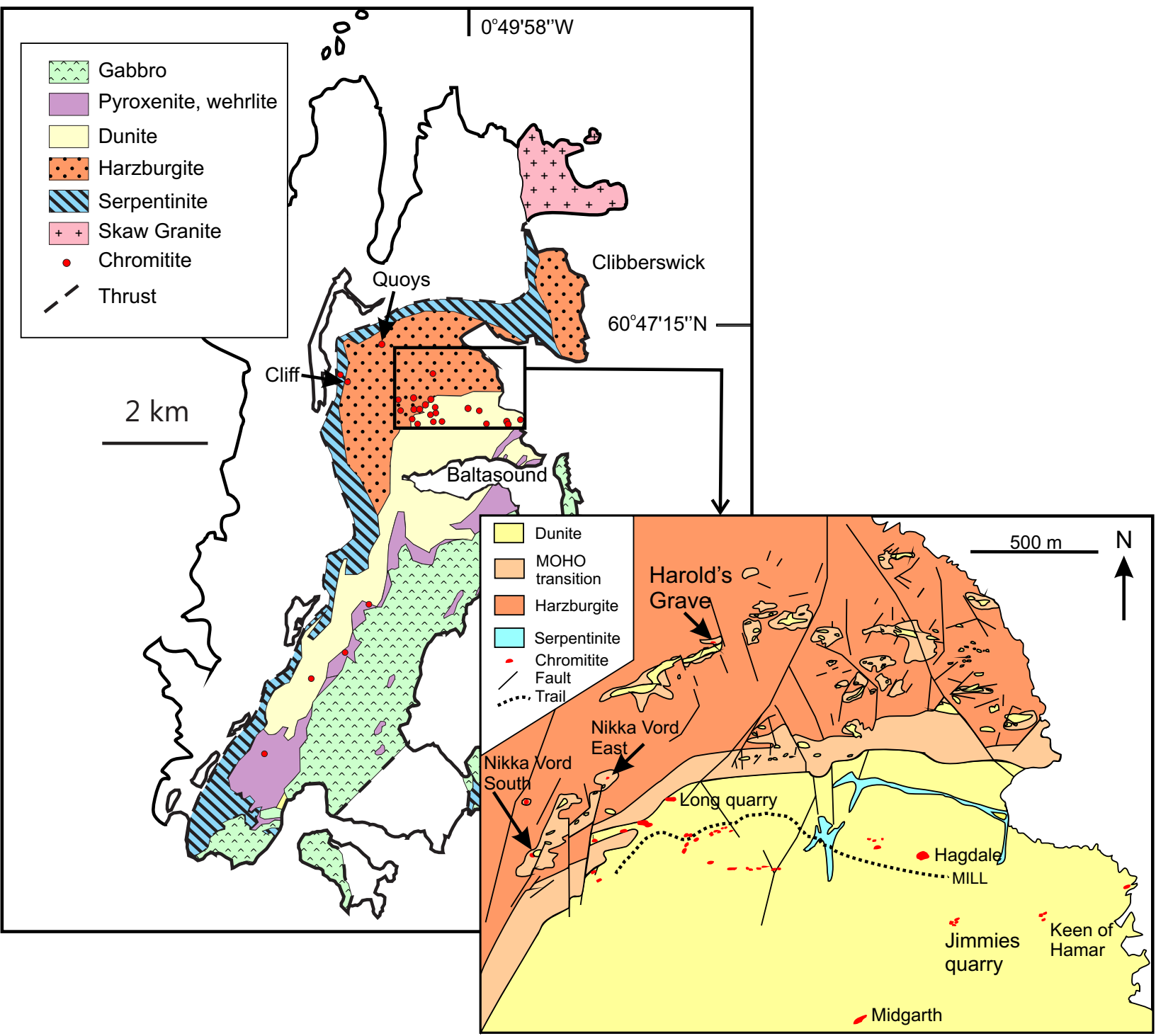


Figure 2

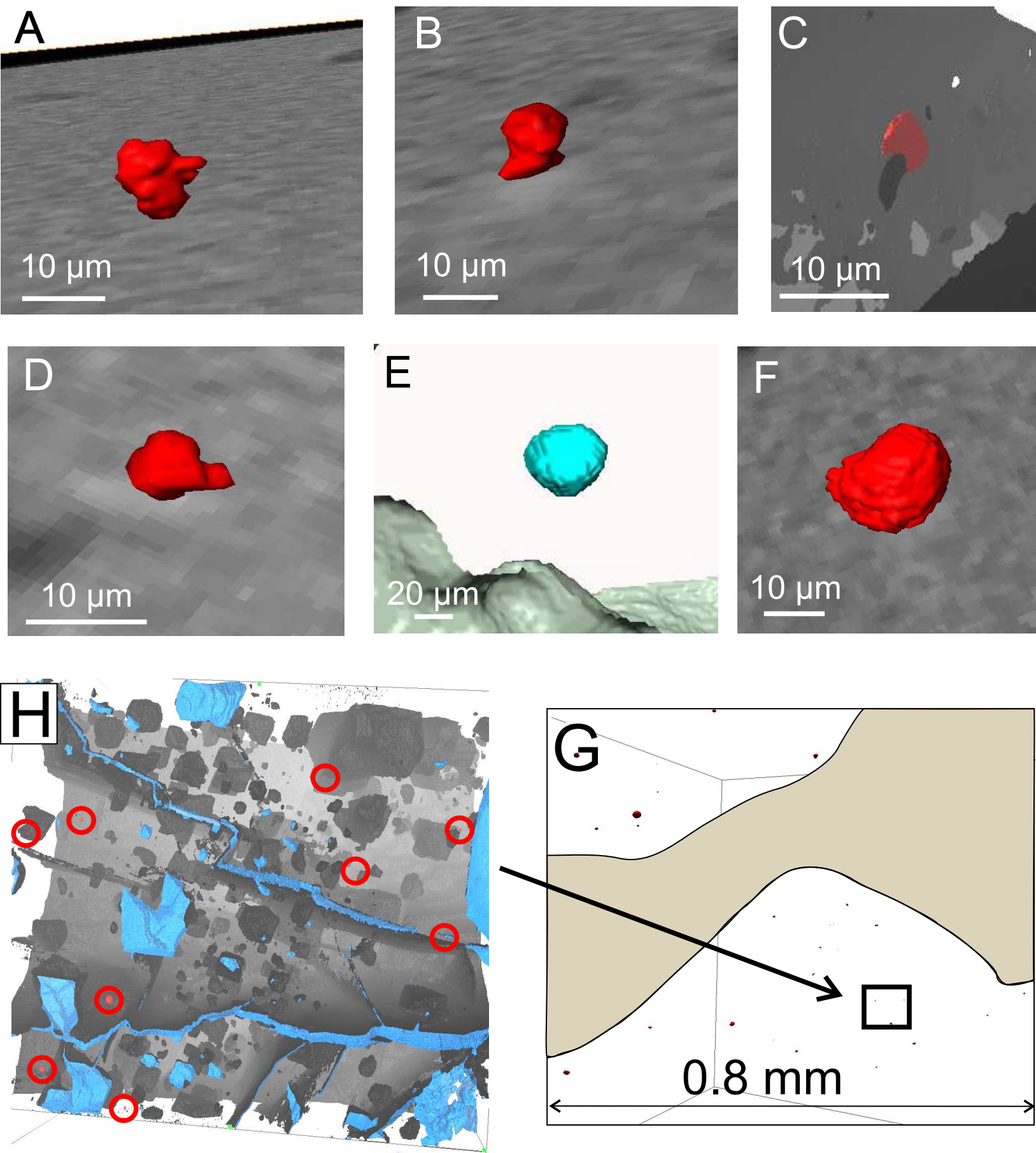


Figure 3

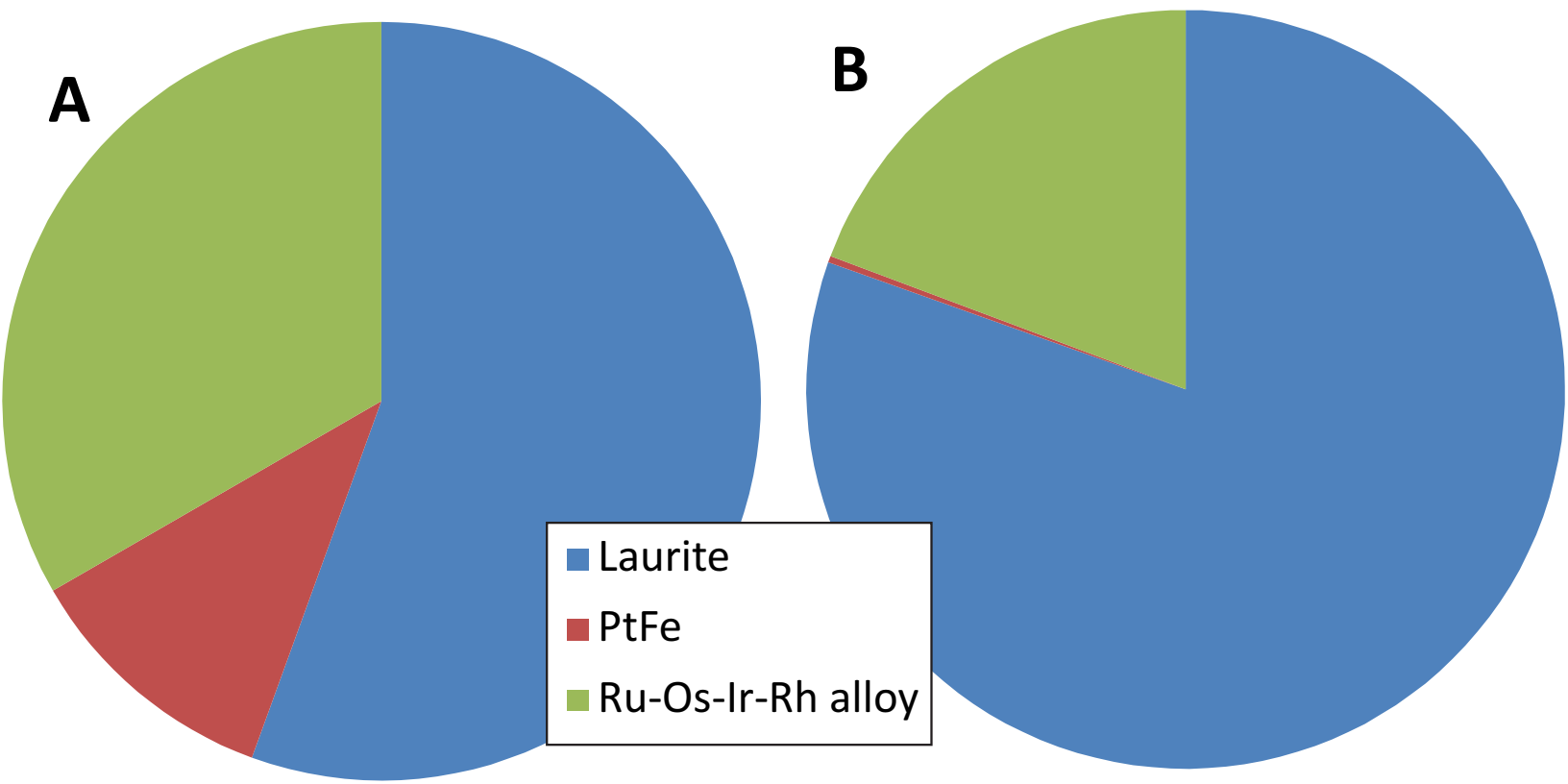


Figure 4

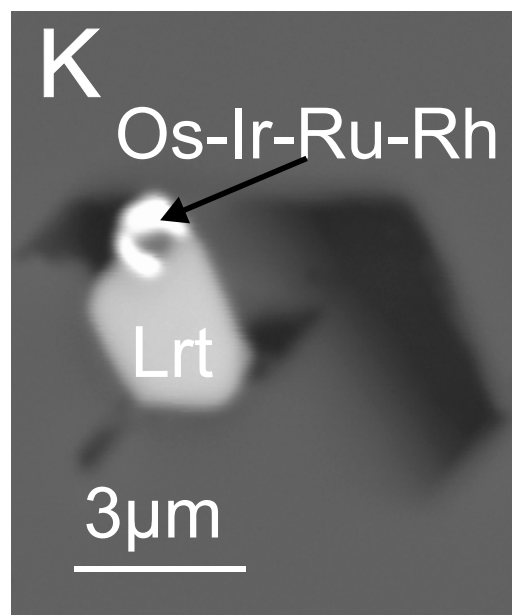
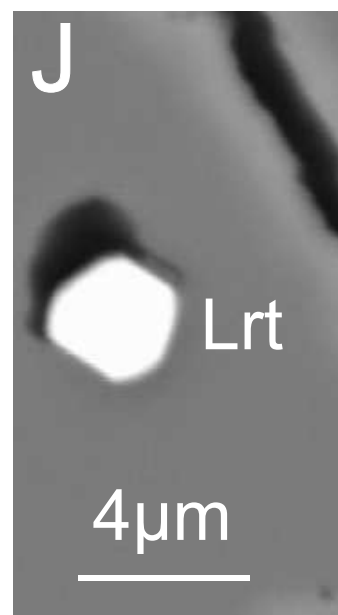
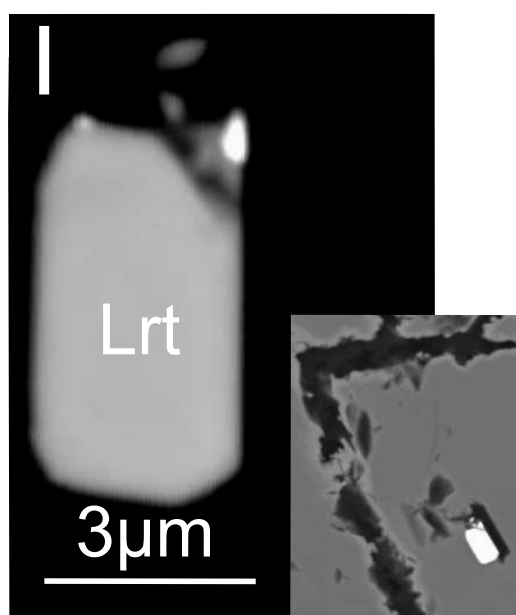
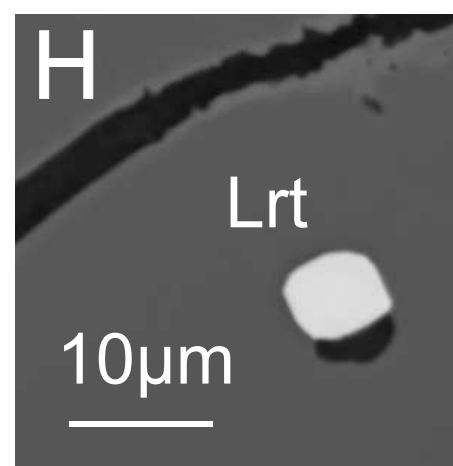
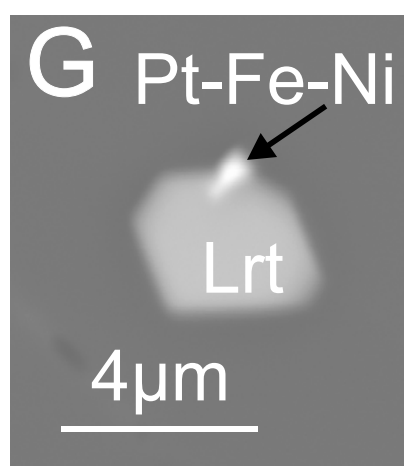
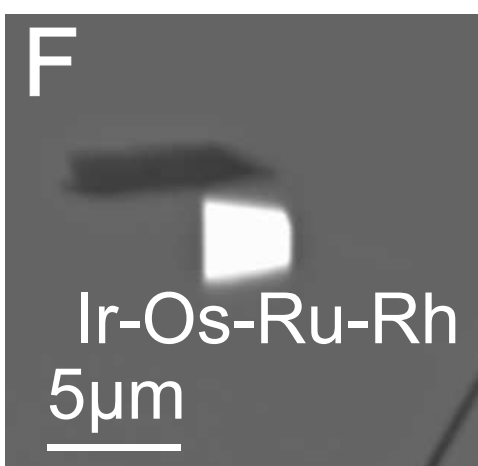
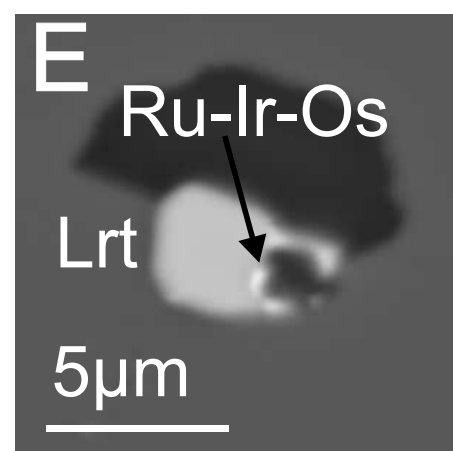
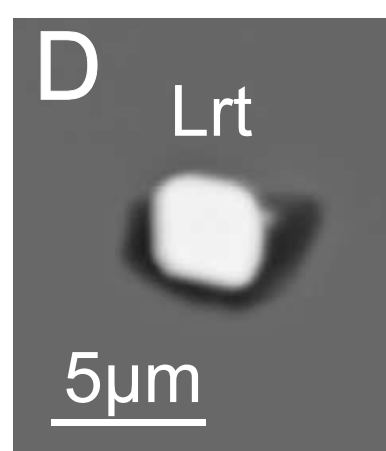
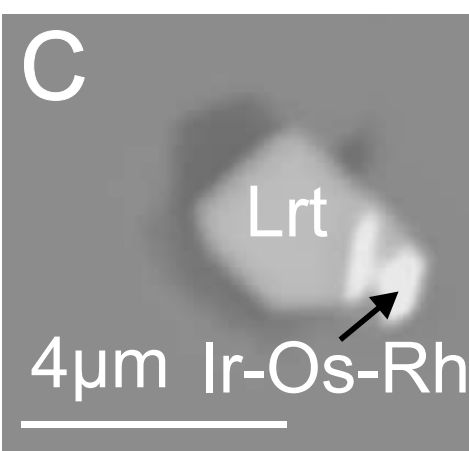
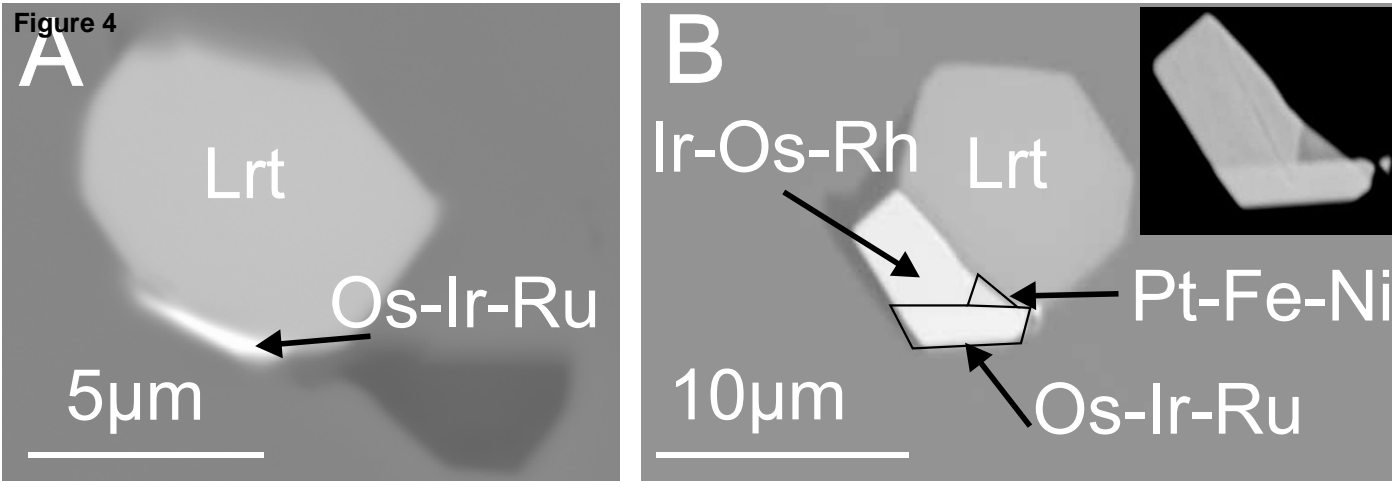


Figure 5

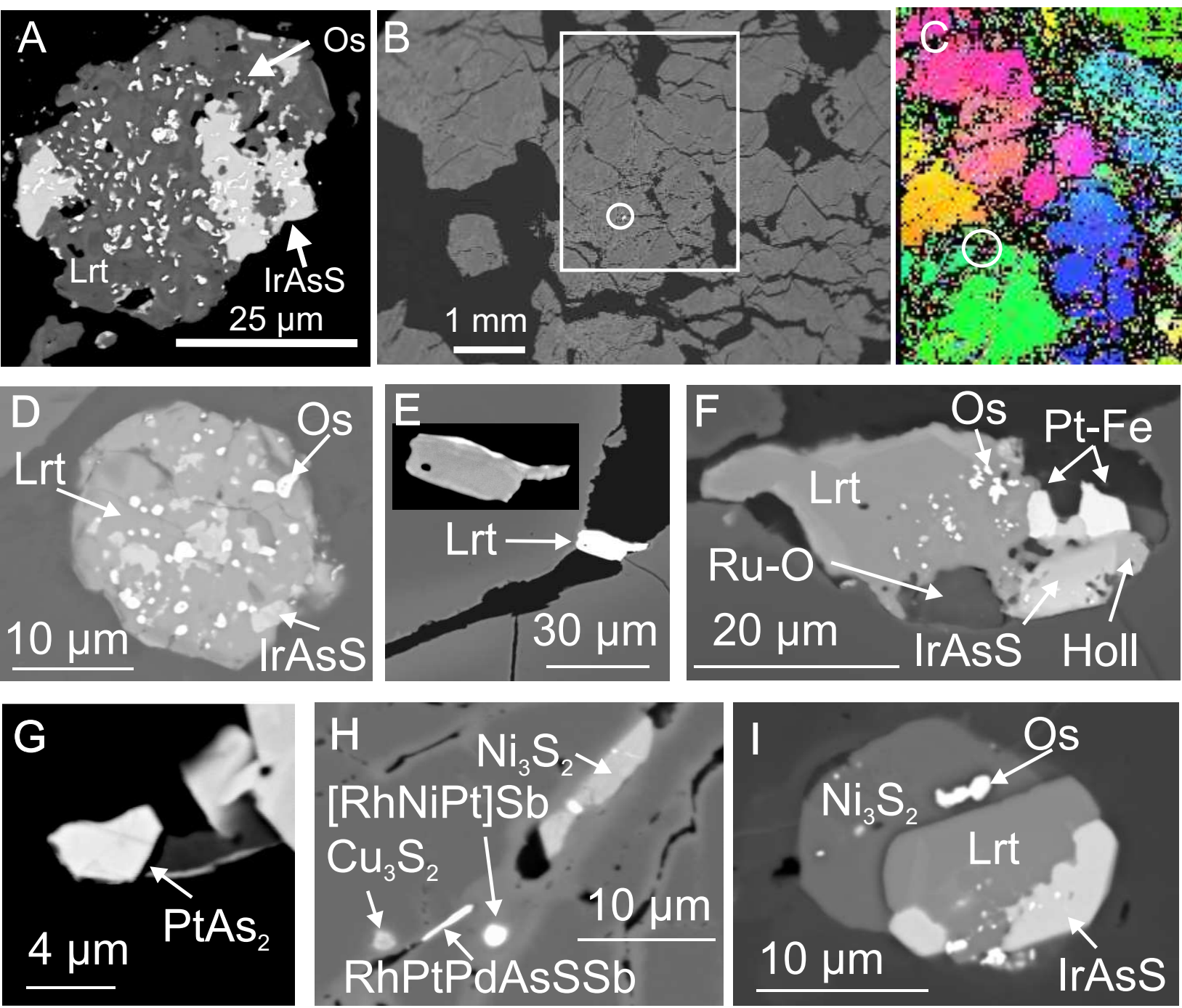


Figure 6

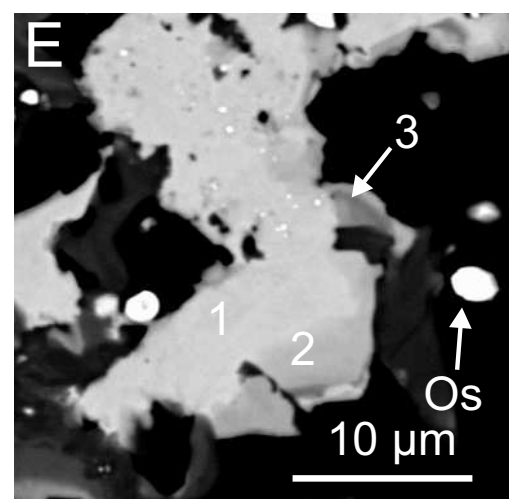
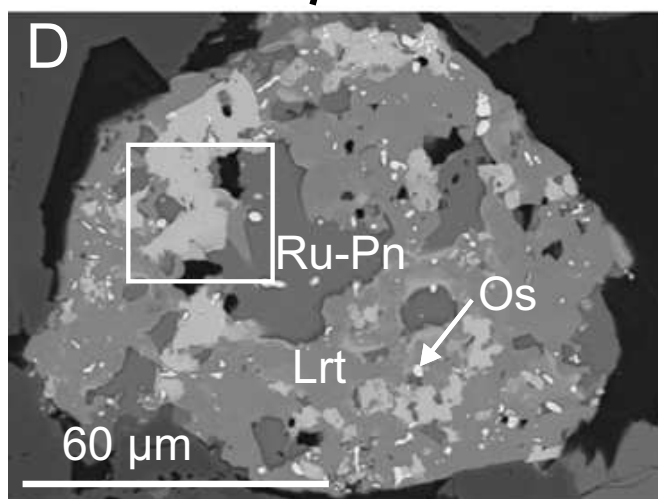
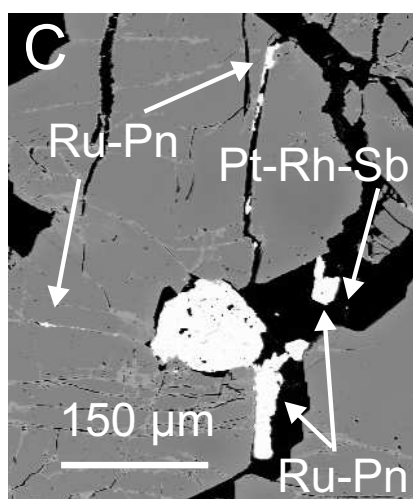
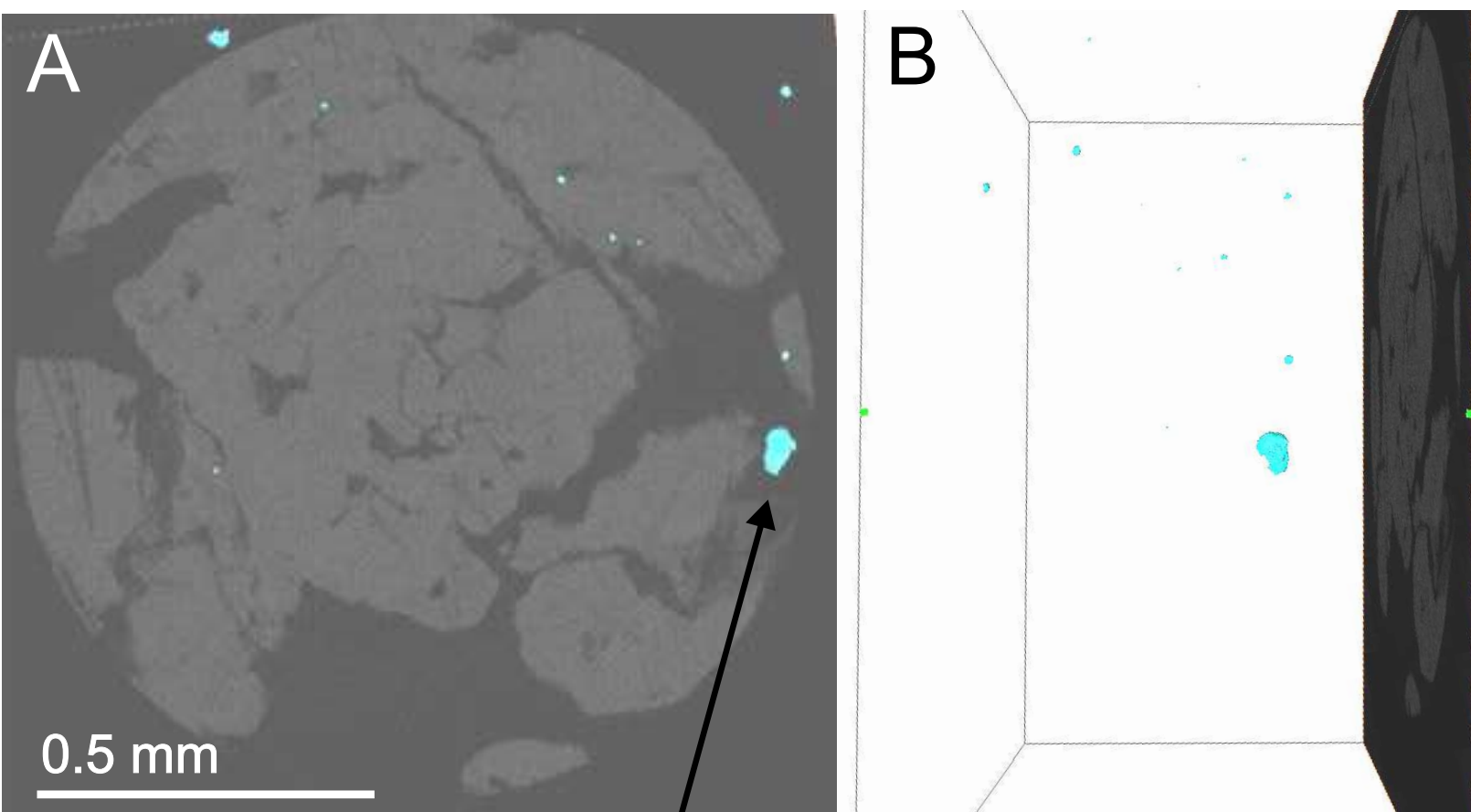


Figure 7

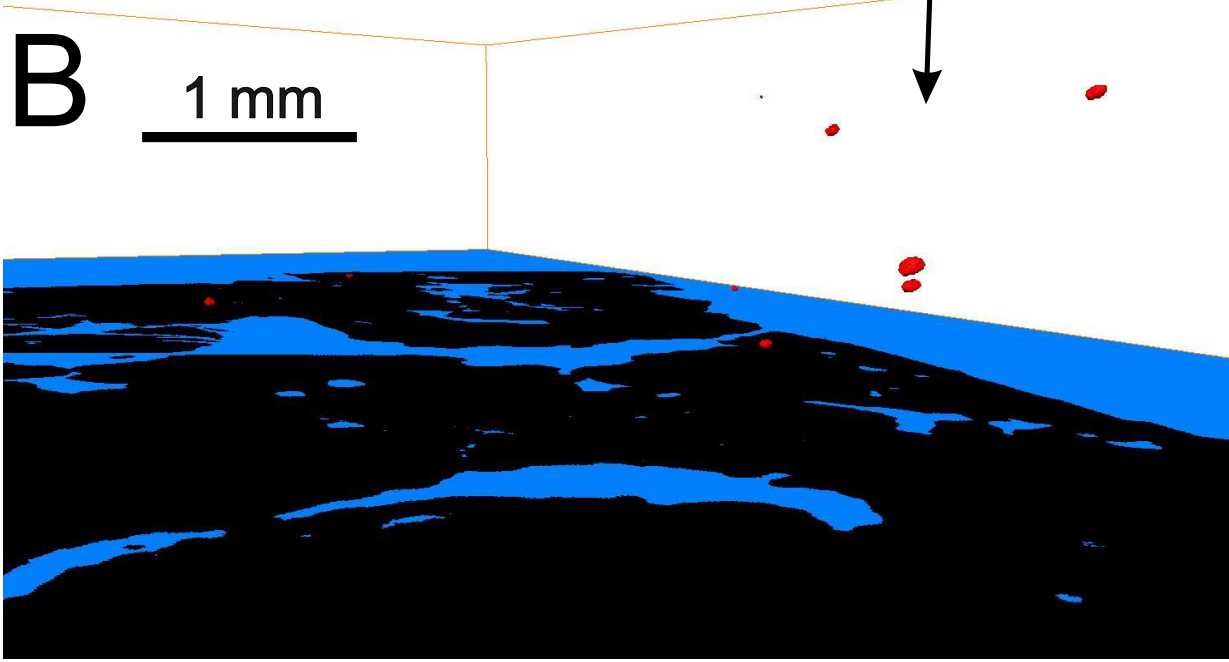
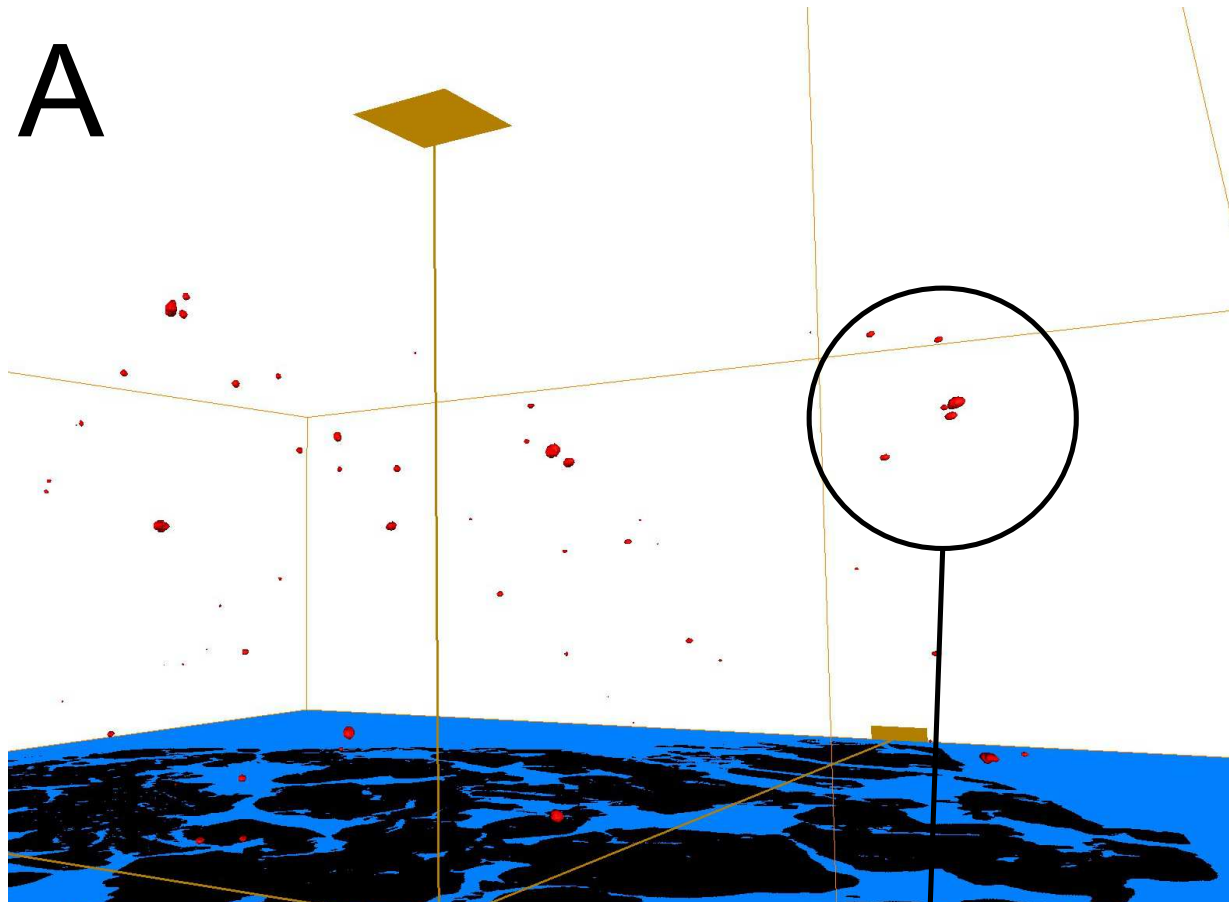


Figure 8

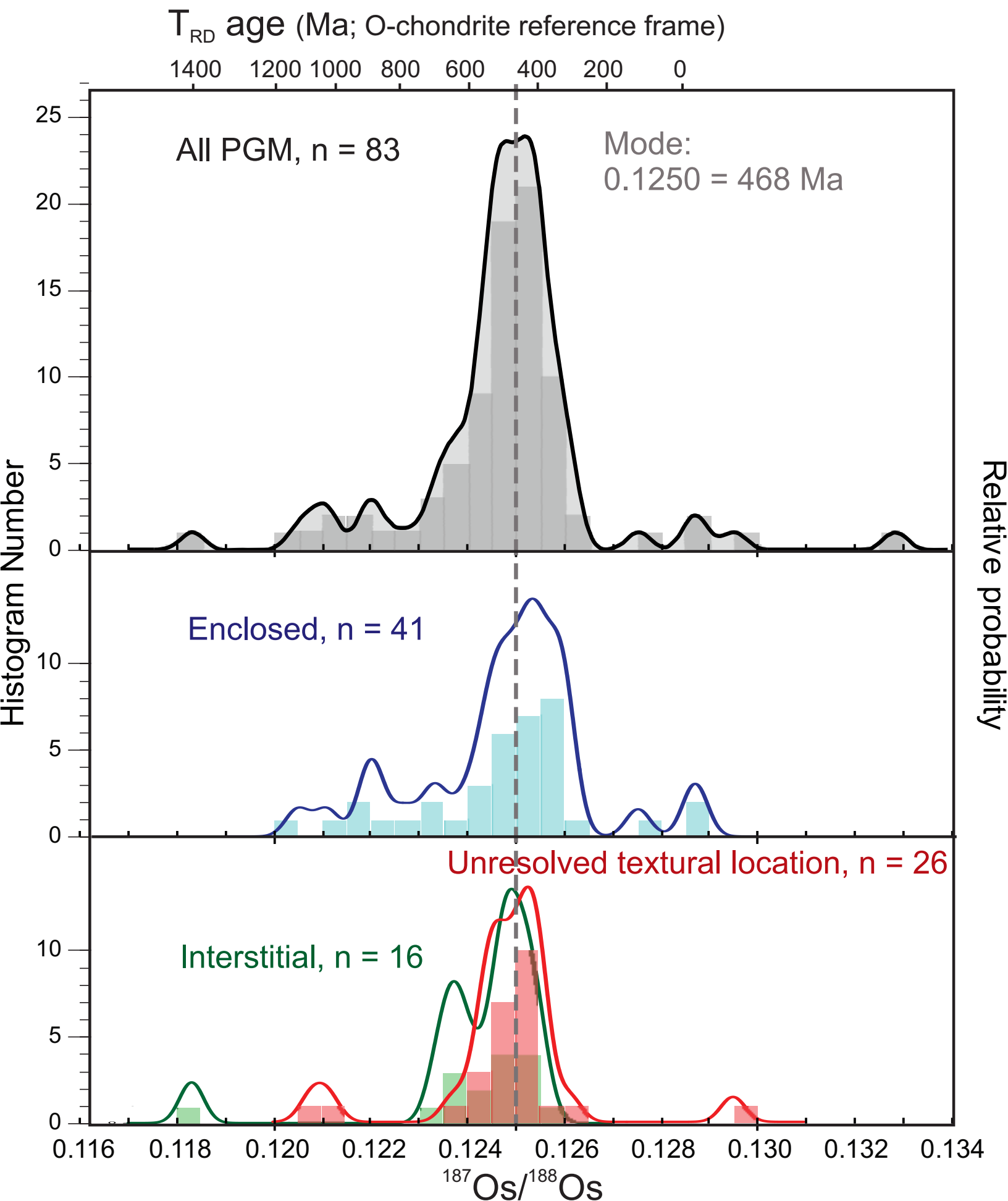
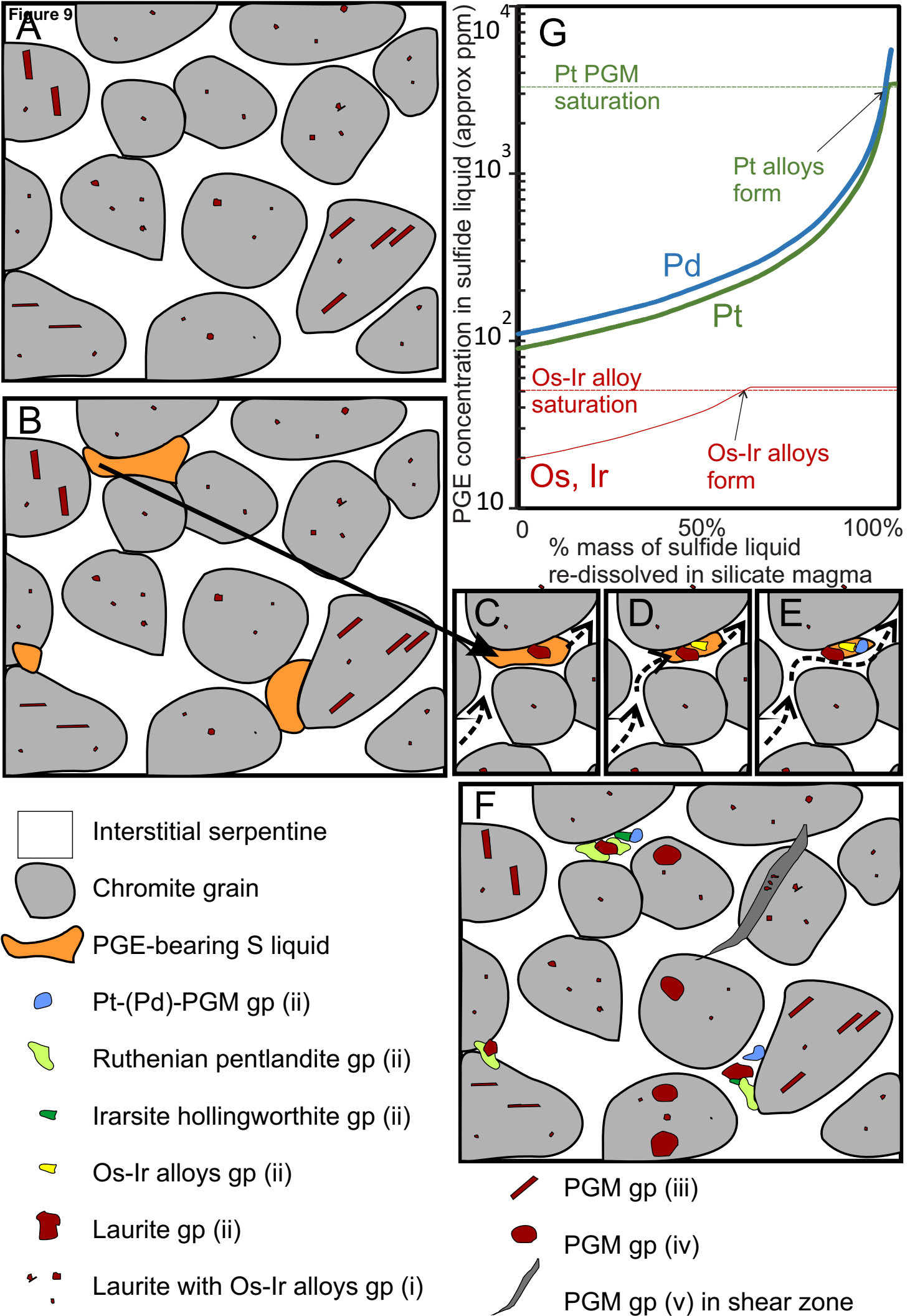


Figure 9



Supplementary data table S1

[Click here to download Electronic Annex: Table Supp S1 HRXCT_table.xlsx](#)

Supplementary data table S2

[Click here to download Electronic Annex: table Supp S2 HG 2016.docx](#)

Supplementary data table S3

[Click here to download Electronic Annex: table Supp S3 HG 2016.docx](#)

Supplementary data table S4

[Click here to download Electronic Annex: Table Supp S4 Os isotopes_CD.xlsx](#)

Supplementary figure S1

[Click here to download Electronic Annex: Fig. S1 abundance PGM HG1 6 7.eps](#)

Supplementary figure S2

[Click here to download Electronic Annex: Fig. S2 3D big cluster.eps](#)

Supplementary figure S3

[Click here to download Electronic Annex: Fig. S3 HG7 cluster pies.eps](#)

Supplementary figure S4

[Click here to download Electronic Annex: Fig. S4 planar array 3D.eps](#)

Supplementary figure S5

[Click here to download Electronic Annex: Fig. S5 HHG6a 3D.eps](#)

Supplementary figure S6

[Click here to download Electronic Annex: Fig. S6 lowOs SEM.eps](#)

Supplementary figure S7

[Click here to download Electronic Annex: Fig. S7 SEM notHG.eps](#)